Journal of Asian Earth Sciences 160 (2018) 348–364

Contents lists available at ScienceDirect

Journal of Asian Earth Sciences

journal homepage: www.elsevier.com/locate/jseaes

Full length article

The Early Cretaceous bimodal volcanic suite from the Yinshan Block, western North China Craton: Origin, process and geological significance

Pengyuan Guo[a,b,*], Yaoling Niu[a,b,c,d,*], Pu Sun[a,b], Xiaohong Wang[a,b], Hongmei Gong[a,b], Meng Duan[d], Yu Zhang[b], Juanjuan Kong[a,b], Liyan Tian[e], Shiguo Wu[e]

[a] Institute of Oceanology, Chinese Academy of Sciences, Qingdao 266071, China
[b] Laboratory for Marine Geology, Qingdao National Laboratory for Marine Science and Technology, Qingdao 266061, China
[c] Department of Earth Sciences, Durham University, Durham DH1 3LE, UK
[d] School of Earth Science and Mineral Resources, China University of Geosciences, Beijing 100083, China
[e] Institute of Deep-sea Science and Engineering, Chinese Academy of Sciences, Sanya 572000, China

ARTICLE INFO

Keywords:
Bimodal volcanic suite
North China Craton
High $^{87}Sr/^{86}Sr$ ratios
Intra-plate volcanism
Lower crust re-working
Lithosphere thinning

ABSTRACT

We present geochemical and age data for coeval basalt and rhyolite in the Yinshan Block, western North China Craton, to study the origin of the 'Daly Gap' in this bimodal volcanic suite. SHRIMP zircon U-Pb dating for felsic rocks and bulk rock $^{40}Ar/^{39}Ar$ dating for mafic rocks yield their ages of 107–133 Ma. The basalts show elevated abundances of incompatible elements with $[La/Sm]_N$ = 2.65–3.54 and enriched Sr-Nd-Hf isotopic signatures ($^{87}Sr/^{86}Sr(t)$ = 0.7054–0.7084, $^{143}Nd/^{144}Nd(t)$ = 0.5119–0.5123, $^{176}Hf/^{177}Hf(t)$ = 0.2824–0.2826), consistent with their derivation from low degree melting of previously metasomatized lithospheric mantle. The rhyolites display similar enrichment in alkalis and other incompatible elements, but have obvious Nb-Ta depletion. Combined with their more enriched Nd-Hf isotopic compositions ($\varepsilon_{Nd}(t) = -12$ to -18, $\varepsilon_{Hf}(t) = -2$ to -14), these rhyolites are inferred to have been generated by mixing of the mantle-derived basaltic magma with felsic melts derived from lower continental crust anataxis induced by the basaltic magma. Furthermore, the extremely low Ba, Sr, Eu contents, high Rb/Sr ratios and unexpectedly high $^{87}Sr/^{86}Sr$ (0.7920–0.7159) in these felsic samples also suggests that their parental magma experienced protracted fractional crystallization of plagioclase (K-feldspar to a lesser extent) *en route to* the surface. This rock association and the unique geochemical characteristics of these volcanic rocks offer a new view on the petrogenesis of bimodal volcanism: the mafic rocks originated from partial melting of the ancient lithospheric mantle. Underplating of the basaltic magmas triggered melting of lower continental crust. The extensive fractional crystallization of the hybridized magma resulted in the highly fractionated rhyolites. This mechanism explains the "Daly Gap" exhibited in this rock association in a continental setting and also the observation that both the lithospheric mantle and crust in East China are thinner than that in West China.

1. Introduction

As frequently reported, the compositional gap between the two end-members of bimodal volcanic suites is known as the 'Daly Gap' (Chayes, 1963; Cann, 1968; Clague, 1978; Bonnefoi et al., 1995). Bimodal volcanism occurs in many tectonic settings, including continental rifts (e.g., Mazzarini et al., 2004; Peccerillo et al., 2007), within plate environments (e.g., Marzoli et al., 1999; Van Wagoner et al., 2002), intra-oceanic islands (e.g., Lacasse et al., 2007), back arc rifts (e.g., Shinjo and Kato, 2000), post-collisional extensional regimes (Aydin et al., 2014), island arcs and continental arcs (e.g., Petrinovic et al., 2006; Zhang et al., 2011; Zhu et al., 2012). Although such bimodal distribution of igneous rocks is common, the dearth of intermediate magmatic compositions in terms of SiO_2 remains a major conceptual issue in igneous petrology (Peccerillo et al., 2003; Ferla and Meli, 2006; Shellnutt et al., 2009; Shao et al., 2015; Liu et al., 2016). However, Niu et al. (2013) considered that the 'Daly Gap' is not as puzzling as widely thought, but is a straightforward consequence of basaltic magma evolution or can be produced during crustal melting induced by mantle-derived basaltic magmas.

Here we present a case study on the origin of the bimodal alkaline volcanic suite from the Yinshan Block, western North China Craton (NCC). The new data suggest that the basaltic magma was produced by partial melting of the lithospheric mantle, while the anatexis of the

* Corresponding authors at: Institute of Oceanology, Chinese Academy of Sciences, Nanhai Road 7, Qingdao, Shandong 266071, China.
E-mail addresses: guopy@qdio.ac.cn (P. Guo), yaoling.niu@durham.ac.uk (Y. Niu).

http://dx.doi.org/10.1016/j.jseaes.2017.10.023
Received 2 August 2017; Received in revised form 21 October 2017; Accepted 22 October 2017
Available online 26 October 2017

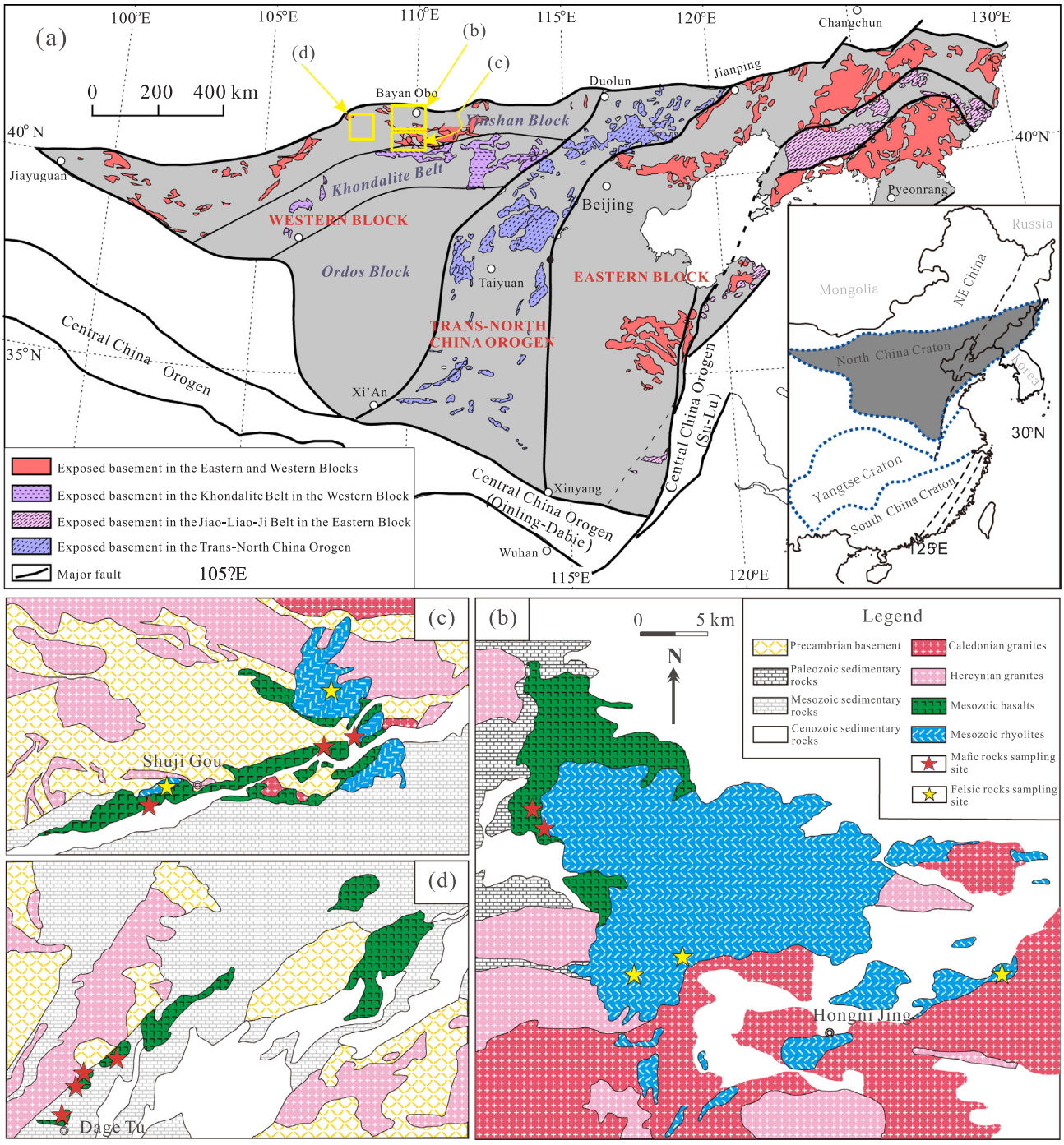

Fig. 1. (a) Sketch map of major tectonic divisions of the North China Craton. (modified from Zhao et al., 2005). (b) (c) (d) The distribution and sample locations of Early Cretaceous volcanic rocks from Yinshan Block.

lower crust induced by the underplating of such basaltic magma produced the more felsic magma, whose protracted crystal fractionation led to the alkaline rhyolite in the Yinshan Block. This model well explains the petrogenesis of the bimodal volcanic suite from the Yinshan Block using the straightforward concept of basaltic magma generation and evolution as suggested by Niu et al. (2013). This study also supports our previous proposal that the lithosphere thinning also occurred in the western NCC (Guo et al., 2014), and provides further insights into the destruction of the NCC.

2. Geological background and samples

The North China Craton (NCC) has been divided into the eastern and western blocks separated by the Trans-North China Orogen (TNCO; Zhao et al., 2005) (Fig. 1a). It has been widely accepted that the ancient (~2.5 Ga), thick (> 200 km) and cold (~40 mW/m^2) lithospheric keel beneath the Eastern NCC (Fig. 1a) had been replaced by young, thin (< 80 km) and hot (> 60 mW/m^2) lithospheric mantle in the Mesozoic (Menzies et al., 1993; Griffin et al., 1998; Fan et al., 2000; Xu, 2001; Gao et al., 2002; Niu, 2005), which explains why the lithosphere beneath eastern NCC is thinner than beneath the other cratons (e.g., Kaapvaal Craton and Zimbabwe Craton in South Africa, Slave Craton in

North America and Siberia Craton; Carlson et al., 2005). On the other hand, the crust in West China is also thicker than in East China (Gao et al., 1998a; Li and Mooney, 1998; Li et al., 2006a), making a coupled relationship between the crust and the mantle lithosphere. However, this first-order observation has never been properly explained. Lower crust delamination beneath the NCC was once proposed as the mechanism to explain the above observation (Gao et al., 2002, 2004). However, the widespread mantle xenoliths in Cenozoic alkaline basalts (e.g., Zheng et al., 2006; Tang et al., 2008) manifest the presence of the lithospheric mantle, excluding the possibility of lower crust foundering into the even denser asthenospheric mantle (Niu, 2014). In fact, the answer to why the crust in West China is thicker than that in East China may hold promise for understanding the NCC destruction. While most people focused on the lithosphere thinning of the eastern block (e.g., Fan et al., 2001; Zhang et al., 2002, 2003; Liu et al., 2008; Gao et al., 1998a,b; Yang and Li, 2008), the lithosphere evolution of the western NCC has been rarely discussed until recently (Guo et al., 2014).

The Mesozoic volcanic rocks in the western NCC are widespread, including localities such as the Erlian Basin (Chen et al., 2009), Siziwang Qi (Zhang et al., 2005; He et al., 2013; Guo et al., 2014), Wuchuan and Guyang Basins (Xu et al., 2014), Baoyintu Swell in Yinshan Block and Heishitougou in the Ordos basin (Zou et al., 2008). These volcanic rocks, dominated by mafic-intermedium compositions with minor felsic volcanic assemblages, are considered as the byproducts of lithosphere thinning (e.g., Guo et al., 2014). These Mesozoic volcanic rocks are usually interbedded with sandstones and conglomerates, and are divided into the Bainvyangpan Formation in the Baoyintu Swell, the Guyang Formation in the Guyang Basin and Wuchuan Basin, with varying thickness of 50–500 m and 1350–3910 m, respectively.

We collected fresh and representative samples from the Guyang Basin (Fig. 1b, c) and Baoyintu Swell (Fig. 1d) in the Yinshan Block. The samples include (1) massive basaltic or basaltic andesitic lava flows with vesicles and/or amygdales and (2) rhyolitic lavas with flow banding. The basaltic samples are mostly aphyric with minor plagioclase phenocrysts (< 3%). The groundmass, with intergranular texture, is made up of microlites of plagioclase, pyroxene, olivine and Fe-Ti oxides. The rhyolites are massive and fresh with porphyritic and fluidal structures. The phenocrysts are quartz (with corrosion/absorption features), K-feldspar and, to a lesser extent, plagioclase. The matrix is mainly cryptocrystalline. Table 1 summarizes sample details.

3. Analytical techniques

3.1. Geochronology

Zircon U-Pb dating. Zircon crystals from felsic rocks were separated using magnetic and heavy liquid methods. Selected zircon grains were mounted in epoxy resin, and then polished to expose their interiors. All the mounted zircon grains were examined petrographically under reflected and transmitted light, and imaged using Cathodoluminescence (CL) to reveal their internal structures. Zircon dating was done using the SHRIMP IIe ion microprobe at the Beijing SHRIMP Centre, Institute of Geology, Chinese Academy of Geological Sciences. The analytical procedure follows Williams (1998). Mass resolution during the analytical sessions was ~5000 (1% definition), and the intensity of the primary ion beam was ~2 nA. Primary beam size was 25–30 μm, and each site was rastered for ~210 s prior to analysis. U abundance was calibrated using the standard M257 (U = 840 ppm, Williams, 1998) and $^{206}Pb/^{238}U$ was calibrated using the standard TEMORA ($^{206}Pb/^{238}U$ age = 417 Ma; Black et al., 2003). Measured compositions were corrected for common Pb using nonradiogenic ^{204}Pb. The U − Pb zircon analyses are presented in Fig. 2 with complete data given in Table 2.

Bulk-rock $^{40}Ar/^{39}Ar$ dating. Fresh basaltic samples were selected for dating. They were crushed into ~1 mm size grains and washed in distilled water. About ~10 such groundmass grains picked under a binocular microscope were irradiated for approximately 30 h at the reactor in the Institute for Nuclear Physics and Chemistry, China Academy of Engineering Physics, Mianyang, using the Chinese Standard Sample of ZBH2506 (biotite, 132.7 Ma) as a flux monitor. Following a decay period of 3 months after irradiation, samples were analyzed in China University of Geosciences (Wuhan) using Argus VI mass spectrometer following Qiu et al. (2015). Argon gas was extracted from the samples by step heating using a MIR10 CO_2 continuing laser. The released gasses were purified by using 3 Zr/Al getter pumps operated for 5–8 min at room temperature and 400 °C, respectively. The data were corrected for system blanks, mass discrimination, and interfering neutron reactions with Ca, Cl, and K. The $^{40}Ar/^{39}Ar$ dating results were calculated using the ArArCALC software (Koppers, 2002). The $^{40}Ar/^{39}Ar$ analytical data are presented as plateau age and isochron age plots (Fig. 3) with complete data given in Table 3.

3.2. Geochemistry

A total of 19 fresh samples (11 basalts and 8 rhyolites) were selected for geochemical analysis. Weathered surfaces, pen marks and saw marks on all samples were removed. Samples that have obvious phenocrysts were crushed into grains of ~0.5–1.0 mm size to painstakingly remove phenocrysts under a binocular with the aim of obtaining melt compositions best represented by the fresh matrix. Aphyric samples without phenocrysts were directly reduced to ~0.5–1.0 mm size grains. All these grains were then ultrasonically-cleaned with Milli-Q water and dried in a clean environment before complete dissolution and analysis.

Major element analysis was done using a Leeman Prodigy inductively coupled plasma-optical emission spectroscopy (ICP-OES) system in the Tianjin Institute of Geology and Mineral Resources. Whole rock trace elements were analyzed using Agilent-7900 inductively coupled plasma mass spectrometer (ICP-MS) in Institute of Oceanology, Chinese Academy of Sciences following Chen et al. (2017). Fifty milligram of each sample was dissolved with an acid mix of Lefort aqua regia (1HCl: $3HNO_3$) and HF in a high-pressure bomb for 15 h, and then re-dissolved with distilled 20% HNO_3 for 2 h till complete dissolution. International rock standard BCR-2 was used to monitor the analytical accuracy and precision. Analytical accuracy, as indicated by relative difference between measured and recommended values, is better than 5% for most elements. The analytical data are given in Table 4.

Sr-Nd-Hf isotopic analysis was done on a Finnigan Neptune Plus MC-ICP-MS at Guangzhou Institute of Geochemistry, Chinese Academy of Sciences following Li et al. (2016b). Our samples were dissolved in distilled HF + HNO_3 at 120 °C for a week. Sr and Nd were separated using conventional ion exchange columns, and the Nd fractions were further separated by using HDEHP columns. The measured $^{87}Sr/^{86}Sr$ and $^{143}Nd/^{144}Nd$ ratios were corrected for mass-fractionation using $^{86}Sr/^{88}Sr = 0.1194$ and $^{146}Nd/^{144}Nd = 0.7219$, respectively. During the analysis, the measured values for NBS-987 Sr standard and JNdi-1 Nd standard is $^{87}Sr/^{86}Sr = 0.710251 \pm 8$ ($N = 5$, 2SD) and $^{143}Nd/^{144}Nd = 0.512096 \pm 4$ ($N = 5$, 2SD), respectively. Hf was separated by using a modified single-column separation procedure by ion exchange using Ln-Spec resin. A detailed analytical procedure is reported in Li et al. (2016b). The $^{176}Hf/^{177}Hf$ ratios were normalized to $^{179}Hf/^{177}Hf = 0.7325$. During Hf isotope analysis, the measured values for JMC-475 Hf standard is $^{176}Hf/^{177}Hf = 0.282185 \pm 5$ ($N = 8$, 2SD). The USGS reference material BHVO-2 run with our samples yields $^{87}Sr/^{86}Sr = 0.703474 \pm 9$, $^{143}Nd/^{144}Nd = 0.512954 \pm 5$ and $^{176}Hf/^{177}Hf = 0.283070 \pm 5$. The analytical data are given in Table 5.

4. Results

4.1. Age data

Zircons from rhyolitic samples are generally transparent, light-brown to colorless grains or grain fragments with anhedral to subhedral

Table 1
Detailed description of Early Cretaceous bimodal volcanic rocks from the Yinshan Block.

Sample	Rock type	Location	GPS	Brief petrography
GY14-02	Rhyolite	Guyang	N41°25′52.9″, E109°58′31.8″	Massive and fresh; fluidal structure and porphyritic; ~5% phenocryst of quartz (~2 mm); ~95% groundmass of cryptocrystalline
GY14-03	Rhyolite	Guyang	N41°25′52.9″, E109°58′31.8″	Massive and fresh; totally cryptocrystalline
GY14-12	Rhyolite	Guyang	N41°12′43.6″, E109°41′03.8″	Massive and fresh; fluidal structure and porphyritic; ~20% phenocryst of quartz (1–2 mm) and ~80% groundmass of cryptocrystalline
GY14-30	Rhyolite	Guyang	N41°26′27.4″, E109°43′40.3″	Massive and fresh; porphyritic; ~8% phenocryst of orthoclase, ~92% groundmass of cryptocrystalline
GY14-32	Rhyolite	Guyang	N41°27′24.6″, E109°43′58.9″	Porphyritic and slightly altered; phenocrysts contains ~15% K-feldspar (1–5 mm) and ~10% quartz (mostly 2 mm); groundmass of plagioclase (~75%)
GY14-34	Rhyolite	Guyang	N41°26′31.5″, E109°40′15.3″	Massive and fresh; fluidal structure and porphyritic; ~5% phenocryst of quartz (~3 mm); ~95% groundmass of cryptocrystalline
GY14-35	Rhyolite	Guyang	N41°26′31.5″, E109°40′15.3″	Massive and fresh; fluidal structure and porphyritic; ~8% phenocryst of quartz (~2–4 mm); ~92% groundmass of cryptocrystalline
GY14-36	Rhyolite	Guyang	N41°26′31.5″, E109°40′15.3″	Massive and altered; fluidal structure and porphyritic; ~15% phenocryst of K-feldspar (~2–4 mm); ~85% groundmass of cryptocrystalline
GY14-15	Basalt	Guyang	N41°09′47.5″, E109°37′06.2″	Massive and fresh; cryptocrystalline texture; plagioclase (~80%), olivine (~10%), magnetite (~10%)
GY14-17	Basalt	Guyang	N41°11′07.4″, E109°38′56.7″	Porphyritic and fresh; ~5% phenocrysts of feldspar (2 mm on average); groundmass contains plagioclase (~80%), clinopyroxene (~5%) and Fe-Ti oxides (~10%)
GY14-27	Basalt	Guyang	N41°10′07.6″, E109°27′00.8″	Porphyritic. ~15% phenocrysts of plagioclase (~4 mm); groundmass contains plagioclase (~70%), olivine (~10%), Fe-Ti oxides (~5%); the olivine in matrix partly altered to iddingsite
GY14-39	Basalt	Guyang	N41°28′29.0″, E109°35′42.3″	Porphyritic and fresh. Phenocrysts contains ~8% plagioclase (1–4 mm) and ~7% K-feldspar; groundmass contains feldspar (~75%), olivine (~5%), Fe-Ti oxides (~5%)
GY14-43	Basalt	Guyang	N41°28′43.5″, E109°36′01.4″	Porphyritic. ~15% phenocrysts of plagioclase (~4 mm); groundmass contains plagioclase (~70%), olivine (~10%), Fe-Ti oxides (~5%); most clinopyroxene in matrix altered to iddingsite
HQ14-01	Basalt	Wulate Houqi	N41°21′37.4″, E107°33′00.3″	Massive and slightly altered; cryptocrystalline texture; clinopyroxene (~30%), plagioclase (~60%), magnetite (~10%); plagioclase altered to carbonate
HQ14-04	Basalt	Wulate Houqi	N41°31′28.2″, E107°32′28.7″	Porphyritic and slightly altered, olivine altered to iddingsite. ~5% phenocrysts of olivine (~2 mm), ~95% groundmass contains plagioclase (~70%), olivine (~15%), Fe-Ti oxide (~10%)
HQ14-05	Basalt	Wulate Houqi	N41°31′30.1″, E107°32′53.0″	Massive and fresh; cryptocrystalline texture; plagioclase (~70%), quartz (~20%) and Fe-Ti oxide (~10%)
HQ14-08	Basalt	Wulate Houqi	N41°30′28.3″, E107°33′53.1″	Massive and slightly altered; cryptocrystalline texture; olivine (~20%), plagioclase (~75%), magnetite (~5%); olivine altered to iddingsite
HQ14-12	Basalt	Wulate Houqi	N41°33′03.6″, E107°33′22.9″	Porphyritic and altered; ~10% phenocrysts of altered pyroxene (~1 mm) and K-feldspar; groundmass trachytic texture with ~80% feldspar and ~10% pyroxene + magnetite
HQ14-17	Basalt	Wulate Houqi	N41°33′00.7″, E107°36′07.8″	Massive and fresh; hyalopilitic texture; glass (~40%), plagioclase (~50%), clinopyroxene + magnetite (~5%)

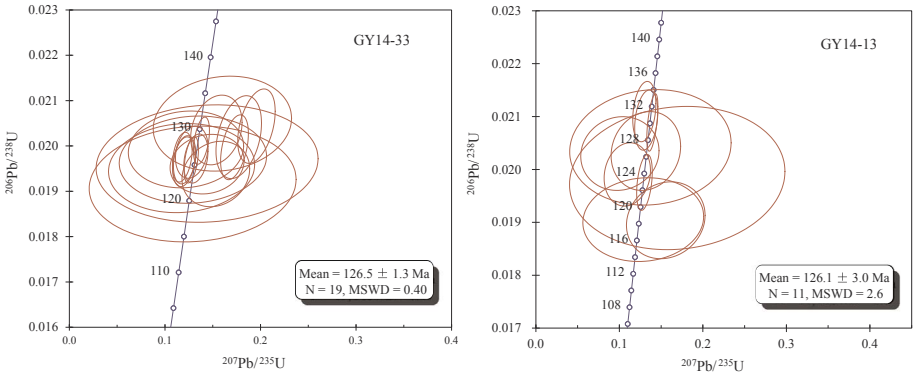

Fig. 2. Concordia diagrams of SHRIMP U–Pb zircon data for the Early Cretaceous felsic rocks from Yinshan Block. Error ellipses are depicted at the 1σ level.

morphology. They are ~60–150 μm in length with length/width ratios of 1:1–2:1. CL images exhibit oscillatory zoning with variable luminescence, indicative of igneous origin. Nineteen analyses of sample GY14-33 zircons show varying U (62–1169 ppm) and Th (35–925 ppm) with Th/U ratios of 0.52–1.04 (Table 1). They gave a weighted mean $^{206}Pb/^{238}U$ age of 126.5 ± 1.3 Ma (MSWD = 0.40) (Fig. 2a). Eleven analyses of sample GY14-13 zircons, with varying U (109–02875 ppm) and Th (96–01816 ppm) and Th/U ratios of 0.15–0.88 (Table 1), form a coherent cluster and yield a weighted mean $^{206}Pb/^{238}U$ age of 126.1 ± 3.0 Ma with MSWD = 2.63 (Fig. 2b). These ages are best interpreted as the formation age of the rhyolite samples. One zircon crystal of sample GY14-13 shows slight discordance, yielding a $^{206}Pb/^{238}U$ age of 2550.7 ± 35.4 Ma (Table 1), which is interpreted as a captured old crustal zircon.

The $^{40}Ar/^{39}Ar$ age data for 4 samples are shown in Fig. 3. The obtained HQ14-01, HQ14-17 and GY14-39 plateaus contain the majority of the total ^{39}Ar released. For sample GY14-15, the obtained plateau (13 out of 18 heating steps) corresponds to 72% of the total ^{39}Ar released, which makes the obtained result also acceptable. The obtained results (Table 2) cover a range of ~26 Myrs, varying between 107.30 ± 0.54 Ma (HQ14-17) and 133.13 ± 0.91 Ma (GY14-15). The plateau age and isochron age are identical within error. We interpret the plateau age spectrum to represent the eruption age of these basaltic rocks.

4.2. Geochemical data

The early Cretaceous volcanic rocks from the Yinshan Block define a compositional spectrum (SiO_2 = 47.16–75.87 wt%), with an apparent 'Daly Gap' (i.e., the paucity of SiO_2 = ~60–64 wt%; Fig. 4), and plot in the fields of trachybasalt, basaltic trachyandesite, trachyandesite and rhyolite in the total alkalis vs. silica (TAS) diagram (Fig. 4). The mafic rocks represent evolved melts with varying SiO_2 (47.16–59.80 wt%), high Al_2O_3 (14.70–18.50 wt%) and low $Mg^{\#}$ (0.31–0.51) ($Mg^{\#} = Mg^{2+}/(Fe^{2+} + Mg^{2+})$). In contrast, the felsic volcanic rocks show higher SiO_2 (74.40–75.50 wt%), lower MgO (0.10–0.29 wt%) and Al_2O_3 (12.00–13.89 wt%) (Fig. 4). Note that one sample (GY14-35) has different major element composition, especially for K_2O, Al_2O_3 and CaO, which is explained as the result of post-magmatic alteration (e.g., carbonation).

In the Chondrite normalized rare earth element diagram, the mafic rocks are characterized by enrichment in light rare earth elements (LREEs) and depletion in heavy rare earth elements (HREEs), with high $[La/Sm]_N$ (2.74–3.73) and basically no Eu anomalies ($Eu/Eu^* = 0.90–1.08$) (Fig. 5a). In primitive mantle normalized multi-element diagram (Fig. 5b), the basalts display incompatible element highly enriched characters with more enrichment in the progressively more incompatible elements, suggesting the more enriched source materials than the primitive mantle. Note that these mafic rocks display no obvious Nb-Ta trough, a marked signature of Mesozoic basalts (> 110 Ma) from the eastern NCC (Liu et al., 2008), most probably because these samples have low Th-U concentrations (Fig. 5b).

The rhyolites have highly varied REEs ($[La/Sm]_N$ = 1.67–8.43) with significant negative Eu anomalies (Eu/Eu^* = 0.01–0.55) (Fig. 5c). Fig. 5d shows these samples in the primitive mantle normalized multi-element diagram. The extremely low content of Ba-Sr-Eu and P-Ti (Fig. 5d) is consistent with fractional crystallization of plagioclase, apatite and Ti-magnetite during magma ascent from the source region, while the trough at Nb-Ta (Fig. 5d) implies the involvement of continental crust materials in the origin of these rocks (see discussion below).

The initial isotopic ratios of all samples are calculated to 126 Ma of representative sample in this study. The mafic rocks have initial $^{87}Sr/^{86}Sr$ ratios of 0.7054–0.7084. They also have variably low $\varepsilon_{Nd}(t) = -4.82$ to -12.14 and $\varepsilon_{Hf}(t) = -1.73$ to -12.73. All our basaltic samples plot in the region defined by the Mesozoic basalts from East China in both Sr-Nd and Nd-Hf isotope diagrams (Fig. 6). The rhyolites display more enriched Nd-Hf isotopic characters ($\varepsilon_{Nd}(t) = -11.98$ to -17.31; $\varepsilon_{Hf}(t) = -13.19$ to -18.71) when compared with the mafic ones (Fig. 6b), suggesting more enriched source materials. Interestingly, the rhyolites have unexpectedly high $^{87}Sr/^{86}Sr$ ratios, ranging from 0.7159 to 0.7920 (Table 5 and Fig. 7), and their Rb/Sr ratios are higher than those mafic ones by one or two orders of magnitude. Fig. 7 shows that the $^{87}Sr/^{86}Sr$ of the rhyolites correlate well with Rb/Sr, Sr and Eu/Eu^*, indicating that all these parameters are controlled by a common process involving fractional crystallization of plagioclase and K-rich feldspars to a lesser extent. Note that the correlation between $^{87}Sr/^{86}Sr$ and Rb/Sr of the rhyolites gives an isochron age of 128 ± 27 Ma (Fig. 7a), consistent with our age data (see above).

5. Discussion

5.1. Early Cretaceous bimodal volcanism in the western NCC

Mesozoic volcanic rocks are widespread in the western NCC (Fig. 1). They are dominantly basaltic rocks (Zhang et al., 2005; Zou et al., 2008; Chen et al., 2009; He et al., 2013; Guo et al., 2014), with rhyolitic rocks rarely reported (Zhang, 2013). Our four $^{40}Ar/^{39}Ar$ age data on basalt samples show varying ages of 107.30 ± 0.54 Ma to 133.13 ± 0.91 Ma (Fig. 3), consistent with previous $^{40}Ar/^{39}Ar$ ages for the Mesozoic volcanism in the Erdos (126.2 Ma; Zou et al., 2008), Erlian Basin (129.1 Ma; Chen et al., 2009) and Siziwang Qi (108.6–128.4 Ma; Zhang et al., 2005; He et al., 2013). All these basalt age data and the rhyolite zircon U–Pb age data (126.1–126.5 Ma; Fig. 2) indicate an Early Cretaceous bimodal volcanism in the western NCC. Such a close association of basalt and rhyolite in time and space offers convincing evidence that these rocks are different products of the same thermal/magmatic event, which must have lasted for at least ~26 Myrs.

Table 2
Zircon U-Pb SHRIMP analytical data of the felsic lavas from the Yinshan Block.

Spot name	$^{206}Pb^{c}$	U (ppm)	Th (ppm)	$^{232}Th/^{238}U$	$^{206}Pb^{*}$ (ppm)	$^{238}U/^{206}Pb$	± 1σ	$^{207}Pb/^{206}Pb$	± 1σ	$^{207}Pb/^{235}U$	± 1σ	$^{206}Pb/^{238}U$	± 1σ	t-$^{206}Pb/^{238}U$ (Ma)	± 1σ
Sample: GY14-33															
GY14-33-1	0.00	64	35	0.57	1.1	48.93	2.7	0.0695	6.1	0.20	6.6	0.0204	2.7	130.4	3.4
GY14-33-2	1.86	83	67	0.83	1.4	51.51	2.4	0.0574	15.0	0.15	15.2	0.0194	2.4	124.0	3.0
GY14-33-3	0.17	892	925	1.07	15.5	49.70	1.7	0.0498	3.6	0.14	4.0	0.0201	1.7	128.4	2.2
GY14-33-4	0.43	1096	923	0.87	18.6	50.76	1.7	0.0470	3.5	0.13	3.9	0.0197	1.7	125.8	2.1
GY14-33-5	1.34	295	266	0.93	5.0	50.96	2.2	0.0534	17.5	0.14	17.7	0.0196	2.2	125.3	2.7
GY14-33-6	0.21	907	651	0.74	15.4	50.69	1.8	0.0487	6.0	0.13	6.3	0.0197	1.8	125.9	2.2
GY14-33-7	4.78	127	84	0.68	2.3	49.96	2.7	0.0446	32.2	0.12	32.3	0.0200	2.7	127.8	3.4
GY14-33-8	0.42	111	63	0.59	1.9	49.50	3.0	0.0637	8.3	0.18	8.9	0.0202	3.0	128.9	3.8
GY14-33-9	-0.11	157	127	0.84	2.7	50.08	2.4	0.0628	5.0	0.17	5.6	0.0200	2.4	127.5	3.0
GY14-33-10	0.71	158	133	0.87	2.8	49.10	2.5	0.0548	11.2	0.15	11.5	0.0204	2.5	130.0	3.2
GY14-33-11	0.94	1131	848	0.78	19.3	50.84	1.8	0.0443	6.2	0.12	6.5	0.0197	1.8	125.6	2.3
GY14-33-12	0.96	1269	668	0.54	21.8	50.58	1.8	0.0434	5.5	0.12	5.8	0.0198	1.8	126.2	2.3
GY14-33-13	0.76	774	613	0.82	13.3	50.31	1.9	0.0468	8.5	0.13	8.7	0.0199	1.9	126.9	2.4
GY14-33-14	10.13	114	61	0.55	2.2	50.46	4.1	0.0536	52.2	0.15	52.3	0.0198	4.1	126.5	5.1
GY14-33-15	3.13	81	42	0.53	1.5	48.65	3.3	0.0568	29.5	0.16	29.6	0.0206	3.3	131.2	4.2
GY14-33-16	3.92	135	112	0.85	2.4	51.06	3.2	0.0438	42.4	0.12	42.6	0.0196	3.2	125.0	3.9
GY14-33-17	0.90	976	730	0.77	16.7	50.73	1.8	0.0444	6.1	0.12	6.4	0.0197	1.8	125.8	2.2
GY14-33-18	5.66	62	37	0.62	1.1	51.90	4.2	0.0490	54.6	0.13	54.8	0.0193	4.2	123.0	5.1
GY14-33-19	4.64	112	69	0.64	2.0	50.54	3.1	0.0477	38.9	0.13	39.0	0.0198	3.1	126.3	3.9
Sample: GY14-13															
GY14-13-1	11.23	109	96	0.91	2.1	51.11	4.3	0.0637	49.4	0.17	49.5	0.0196	4.3	124.9	5.3
GY14-13-2	1.20	1054	673	0.66	18.7	48.89	1.8	0.0470	6.6	0.13	6.9	0.0205	1.8	130.5	2.4
GY14-13-3	7.43	133	100	0.78	2.5	49.84	3.4	0.0502	45.8	0.14	45.9	0.0201	3.4	128.1	4.3
GY14-13-4	8.38	414	358	0.89	7.3	53.48	2.5	0.0610	19.7	0.16	19.8	0.0187	2.5	119.4	3.0
GY14-13-5	5.04	307	196	0.66	5.5	50.26	2.3	0.0371	30.3	0.10	30.4	0.0199	2.3	127.0	2.8
GY14-13-6	0.39	1265	913	0.75	21.0	51.92	1.8	0.0490	4.4	0.13	4.7	0.0193	1.8	123.0	2.2
GY14-13-7	27.73	2756	1816	0.68	63.0	52.00	2.7	0.0513	36.8	0.14	36.9	0.0192	2.7	122.8	3.3
GY14-13-8	1.95	160	98	0.63	2.8	50.29	2.4	0.0482	20.6	0.13	20.7	0.0199	2.4	126.9	3.1
GY14-13-9	1.44	1254	1067	0.88	22.5	48.49	1.8	0.0458	6.8	0.13	7.0	0.0206	1.8	131.6	2.4
GY14-13-10	0.16	1611	1170	0.75	28.3	49.04	1.8	0.0496	2.6	0.14	3.1	0.0204	1.8	130.1	2.3
GY14-13-11	1.55	432	216	0.52	7.3	51.46	2.0	0.0410	16.5	0.11	16.6	0.0194	2.0	124.1	2.5
GY14-13-12	1.85	2875	443	0.16	1217.4	2.07	1.7	0.1605	0.6	10.71	1.8	0.4838	1.7	2543.8	35.4

Pb^{c} and Pb^{*} indicate the common and radiogenic portions, respectively.

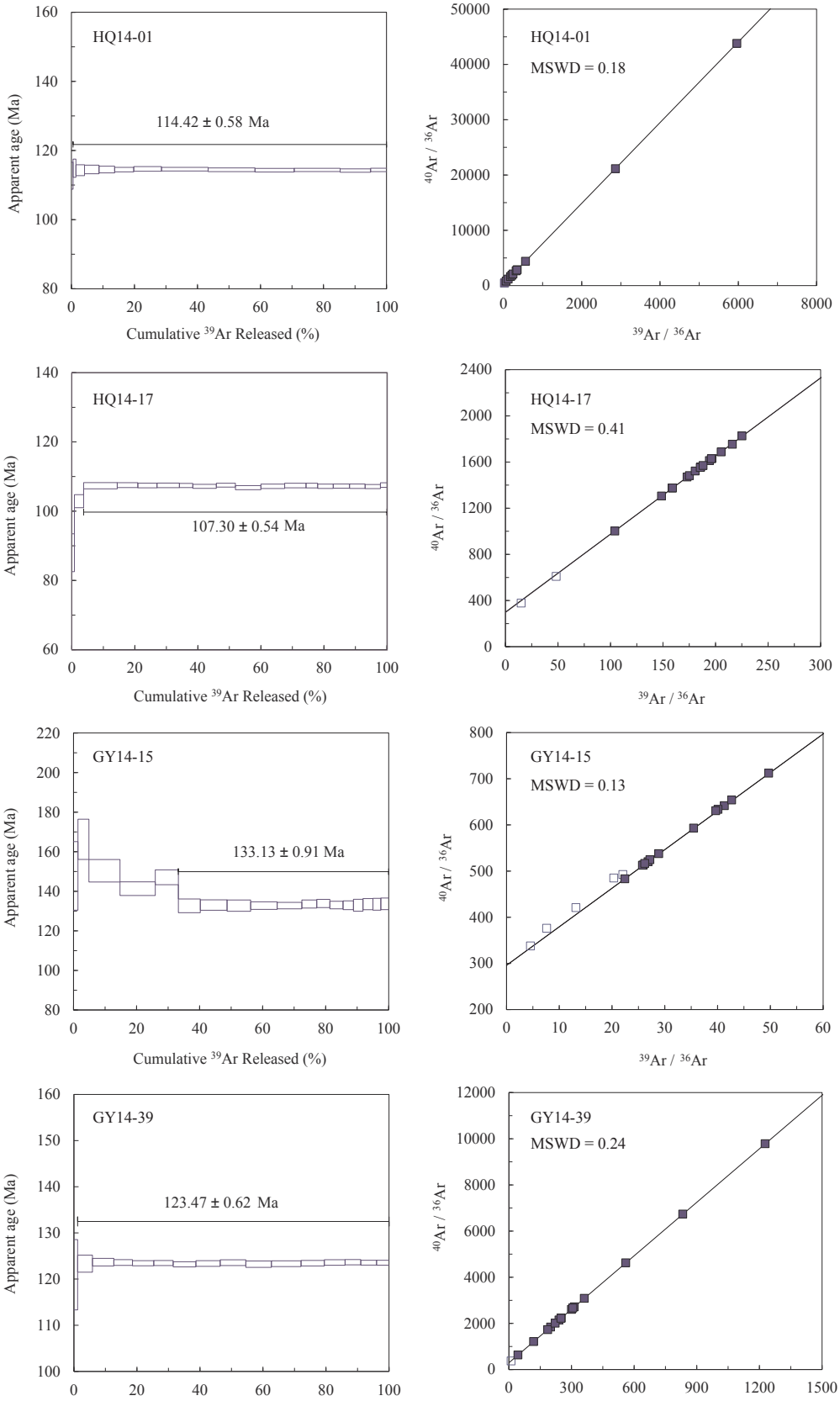

Fig. 3. Ar–Ar age spectra and $^{40}Ar/^{36}Ar$ vs. $^{39}Ar/^{36}Ar$ correlation of the whole rocks of the Early Cretaceous mafic rocks from Yinshan Block.

5.2. Petrogenesis of the basalts

The basalts from the Yinshan Block have varied SiO_2 (47.16–59.80 wt%), low $Mg^{\#}$ (0.31–0.51), Cr (7.74–93.82 ppm) and Ni (15.14–52.11 ppm), indicative of their evolved nature from their mantle-derived parental melts through fractional crystallization. MgO, CaO, $Fe_2O_3^T$, TiO_2 and CaO/Al_2O_3 negatively correlate with SiO_2 (Fig. 4), and this is also the case between SiO_2 and Sc, V, Mn, Co (not

Table 3
$^{40}Ar/^{39}Ar$ dating results of the mafic lavas from the Yinshan Block.

Run ID	Laser (%)	$^{40}Ar/^{39}Ar$	$^{37}Ar/^{39}Ar$	$^{36}Ar/^{39}Ar$	$^{40}Ar^{*}/^{39}Ar_{k}$	$^{40}Ar^{*}$ (%)	^{39}Ark (%)	Age (Ma)	± 2 s (Ma)
Sample HQ14-01 Groundmass J = 0.00894954 ± 0.00002237									
Plateau age = 114.42 ± 0.58 Ma, Total fusion age = 114.43 ± 0.59 Ma									
WHA0367-010	6.6%	20.745351	1.428597	0.046238	7.18534	34.61	0.53	112.70	± 3.91
WHA0367-011	7.2%	16.317052	1.344052	0.030744	7.32937	44.88	0.90	114.89	± 2.64
WHA0367-012	8.0%	11.455443	0.971570	0.014329	7.29074	63.61	2.73	114.30	± 1.58
WHA0367-013	9.0%	9.705266	0.776161	0.008309	7.30506	75.23	4.60	114.52	± 1.23
WHA0367-014	10.0%	8.923904	0.619377	0.005631	7.30361	81.81	4.97	114.50	± 0.96
WHA0367-016	12.0%	8.676828	0.591389	0.004793	7.30199	84.12	6.06	114.47	± 0.65
WHA0367-017	15.0%	8.515255	0.694996	0.004224	7.31632	85.88	8.81	114.69	± 0.67
WHA0367B-001	20.0%	8.224387	0.678168	0.003256	7.31022	88.85	14.79	114.60	± 0.53
WHA0367B-002	25.0%	8.137008	0.755030	0.003016	7.29949	89.67	14.88	114.43	± 0.54
WHA0367B-003	30.0%	8.149740	0.734906	0.003083	7.29086	89.42	12.44	114.30	± 0.52
WHA0367B-004	35.0%	7.819602	0.648801	0.001928	7.29579	93.26	14.56	114.38	± 0.47
WHA0367B-005	40.0%	7.387638	0.534856	0.000476	7.28451	98.57	9.67	114.21	± 0.49
WHA0367B-006	45.0%	7.345708	0.364895	0.000254	7.29549	99.29	5.07	114.37	± 0.49
Sample HQ14-17 Groundmass J = 0.00900946 ± 0.00002252									
Plateau age = 107.3 ± 0.54 Ma, Total fusion age = 107.1 ± 0.55 Ma									
WHA0368B-001	5.0%	25.346356	0.363714	0.067132	5.53427	21.83	0.81	87.99	± 5.47
WHA0368B-002	7.0%	12.618425	0.421699	0.020812	6.49807	51.48	2.94	102.88	± 1.88
WHA0368B-003	8.0%	9.627355	0.501977	0.009725	6.78917	70.50	10.66	107.36	± 0.90
WHA0368B-004	9.0%	8.788832	0.458376	0.006839	6.80006	77.35	6.52	107.53	± 0.71
WHA0368B-005	10.0%	8.502165	0.494324	0.005901	6.79324	79.88	6.09	107.42	± 0.67
WHA0368B-006	12.0%	8.656363	0.545170	0.006426	6.79602	78.48	7.11	107.46	± 0.66
WHA0368D-001	14.0%	8.297409	0.493827	0.005206	6.79380	81.85	4.25	107.43	± 0.61
WHA0368D-002	16.0%	8.215877	0.544779	0.004999	6.77741	82.46	7.46	107.18	± 0.58
WHA0368D-003	18.0%	8.110828	0.514987	0.004563	6.79895	83.80	6.06	107.51	± 0.57
WHA0368D-004	21.0%	8.119074	0.695903	0.004793	6.75234	83.13	8.09	106.79	± 0.59
WHA0368D-005	24.0%	8.463591	0.683292	0.005870	6.77781	80.05	7.54	107.18	± 0.63
WHA0368D-006	27.0%	8.649896	0.696443	0.006453	6.79281	78.50	6.78	107.41	± 0.65
WHA0368F-001	30.0%	8.427007	0.700274	0.005701	6.79232	80.57	3.67	107.41	± 0.67
WHA0368F-002	33.0%	8.367581	0.586657	0.005518	6.77865	80.98	4.97	107.20	± 0.62
WHA0368F-003	36.0%	8.302040	0.609928	0.005293	6.78124	81.65	5.17	107.24	± 0.61
WHA0368F-004	39.0%	8.371636	0.608998	0.005535	6.77921	80.95	4.96	107.21	± 0.63
WHA0368F-005	42.0%	8.342448	0.624000	0.005461	6.77317	81.16	4.85	107.11	± 0.60
WHA0368F-006	45.0%	8.308195	0.613488	0.005245	6.80177	81.84	2.07	107.55	± 0.66
Sample GY14-15 Groundmass J = 0.00908764 ± 0.00002272									
Plateau age = 133.13 ± 0.91 Ma, Total fusion age = 138.09 ± 1.19 Ma									
WHA0369B-001	5.0%	74.443854	2.759748	0.220914	9.37115	12.57	1.39	147.79	± 17.33
WHA0369B-002	7.0%	49.372679	2.229648	0.131787	10.59838	21.44	3.48	166.28	± 10.17
WHA0369B-003	8.0%	31.972070	1.757309	0.076351	9.54141	29.81	9.87	150.37	± 5.68
WHA0369B-004	9.0%	22.335102	1.359386	0.045656	8.94418	40.01	11.18	141.31	± 3.45
WHA0369B-005	10.0%	23.840630	1.408448	0.049476	9.32472	39.08	7.32	147.09	± 3.75
WHA0369B-006	12.0%	21.538240	1.326359	0.044871	8.37620	38.86	6.97	132.66	± 3.46
WHA0369D-001	14.0%	18.631841	1.305214	0.034946	8.40097	45.05	8.49	133.04	± 2.64
WHA0369D-002	16.0%	19.382153	1.448181	0.037585	8.38233	43.21	7.49	132.76	± 2.84
WHA0369D-003	18.0%	15.529249	1.364280	0.024523	8.38282	53.94	8.40	132.76	± 1.93
WHA0369D-004	21.0%	14.320779	1.475064	0.020459	8.38352	58.49	7.84	132.77	± 1.65
WHA0369D-005	24.0%	15.794391	1.567049	0.025294	8.43533	53.36	4.73	133.56	± 2.05
WHA0369D-006	27.0%	15.892562	1.596003	0.025572	8.45341	53.14	4.17	133.84	± 2.07
WHA0369F-001	30.0%	15.313121	1.671722	0.023805	8.40181	54.81	4.17	133.05	± 1.91
WHA0369F-002	33.0%	16.710434	1.732172	0.028574	8.39430	50.18	3.30	132.94	± 2.21
WHA0369F-003	36.0%	19.772164	1.524142	0.038881	8.39485	42.42	3.04	132.95	± 3.00
WHA0369F-004	39.0%	19.290288	1.534259	0.037128	8.43180	43.67	3.15	133.51	± 2.83
WHA0369F-005	42.0%	19.882420	1.507747	0.039142	8.42691	42.34	2.52	133.44	± 2.99
WHA0369F-006	45.0%	19.708121	1.552692	0.038515	8.44123	42.79	2.49	133.65	± 2.94
Sample GY14-39 Groundmass J = 0.00914546 ± 0.00002286									
Plateau age = 123.47 ± 0.62 Ma, Total fusion age = 123.42 ± 0.63 Ma									
WHA0370B-002	7.0%	36.435689	2.746366	0.098390	7.56313	20.72	1.17	120.94	± 7.61
WHA0370B-003	8.0%	14.515764	1.373845	0.023341	7.71848	53.13	4.72	123.34	± 1.85
WHA0370B-004	9.0%	10.233143	0.898955	0.008658	7.73920	75.59	6.77	123.66	± 0.82
WHA0370B-005	10.0%	9.211088	0.794083	0.005190	7.73434	83.93	5.90	123.59	± 0.62
WHA0370B-006	12.0%	8.665709	0.809286	0.003382	7.72439	89.09	6.75	123.43	± 0.55
WHA0370D-001	14.0%	8.542905	0.869151	0.002972	7.72700	90.40	6.16	123.48	± 0.55
WHA0370D-002	16.0%	8.691567	1.022490	0.003574	7.70912	88.64	7.21	123.20	± 0.56
WHA0370D-003	18.0%	8.895191	1.074464	0.004238	7.72043	86.74	7.73	123.37	± 0.61
WHA0370D-004	21.0%	8.958406	1.382141	0.004492	7.73178	86.23	8.12	123.55	± 0.62
WHA0370D-005	24.0%	9.294920	1.563859	0.005747	7.71078	82.88	8.12	123.22	± 0.70
WHA0370D-006	27.0%	9.043628	1.457088	0.004845	7.71799	85.26	9.43	123.34	± 0.62
WHA0370F-001	30.0%	8.905490	1.284710	0.004310	7.72520	86.68	7.38	123.45	± 0.60
WHA0370F-003	36.0%	8.692708	1.732746	0.003670	7.73461	88.88	6.58	123.59	± 0.59
WHA0370F-004	39.0%	8.258546	2.098247	0.002279	7.73881	93.59	4.99	123.66	± 0.57
WHA0370F-005	42.0%	8.079708	1.894512	0.001645	7.73211	95.59	5.00	123.55	± 0.52
WHA0370F-006	45.0%	7.964041	2.148141	0.001319	7.73154	96.95	3.97	123.55	± 0.53

Table 4
Bulk rock major and trace element analysis result on volcanic rocks from the Yinshan Block.

Sample no.	HQ14-01	HQ14-04	HQ14-05	HQ14-08	HQ14-12	HQ14-17	GY14-15	GY14-17	GY14-27	GY14-39
Rock type	Basalt	Basalt	Basalt	Basalt	Basalt	Basalt	Basalt	Basalt	Basalt	Basalt
Major element (wt.%)										
SiO_2	53.20	51.80	59.80	52.90	56.90	57.70	48.07	47.16	49.07	49.90
Al_2O_3	15.05	18.50	14.90	17.30	16.50	16.35	15.36	17.38	16.12	14.70
Fe_2O_3	6.94	9.99	7.80	4.01	3.72	2.88	4.25	4.93	7.17	3.66
FeO	4.82	0.10	0.29	4.33	4.27	4.65	10.54	8.80	6.48	8.12
FeO^T	11.06	9.09	7.31	7.94	7.62	7.24	14.36	13.24	12.93	11.41
CaO	6.46	4.59	3.89	5.56	5.53	4.97	7.72	7.42	6.82	6.30
MgO	3.98	2.60	1.84	4.08	2.56	2.58	3.29	4.93	3.76	3.05
K_2O	2.36	3.9	4.58	3.33	3.59	3.00	1.96	1.61	2.01	2.06
Na_2O	3.62	3.92	3.89	3.96	3.66	4.04	3.80	3.77	4.13	3.68
TiO_2	2.28	2.25	1.57	1.91	1.83	1.74	3.27	2.82	2.84	2.33
P_2O_5	0.73	0.85	0.72	0.85	0.82	0.86	1.10	0.73	1.03	0.62
MnO	0.12	0.09	0.08	0.10	0.12	0.12	0.20	0.16	0.15	0.15
$Mol[(Na^+ + K^+)/Al^{3+}]$	0.57	0.58	0.76	0.59	0.60	0.61	0.55	0.46	0.56	0.56
Trace element (ppm)										
Sc	16.5	15.7	12.8	15.2	14.0	12.1	17.6	18.1	17.1	18.2
Ti	10862	12969	9391	11289	10817	10033	18803	16404	17205	14497
V	129	98.8	39.3	118	105	86.6	169	201	203	192
Cr	93.8	72.9	61.1	79.6	44.7	31.7	11.3	8.70	17.1	7.74
Mn	770	649	625	752	837	855	1340	1175	1022	1217
Co	25.3	22.9	18.7	26.1	18.6	15.1	36.1	42.6	34.4	36.2
Ni	52.1	38.1	34.1	46.5	32.3	19.3	15.2	30.9	25.6	15.1
Rb	74.5	95.8	113.4	82.0	85.5	48.8	33.9	28.5	29.9	44.7
Sr	678	668	488	681	715	1152	802	702	746	603
Y	24.9	27.2	23.9	27.4	29.4	29.6	37.1	29.6	33.7	32.0
Zr	262	314	247	301	364	408	329	239	322	282
Nb	49.2	58.9	43.2	54.8	50.4	52.2	29.8	25.9	29.1	27.2
Cs	0.74	1.08	2.31	0.56	1.72	26.2	0.38	7.59	0.31	1.13
Ba	1015	1293	2773	1095	1319	1601	1219	747	983	743
La	39.2	44.3	38.4	42.8	49.7	53.8	47.6	31.9	47.4	41.3
Ce	82.3	93.8	79.7	90.7	105	113	103	68.2	103	85.9
Pr	10.1	11.5	9.76	11.1	13.1	13.9	13.5	8.61	13.1	10.7
Nd	41.4	46.2	39.5	44.9	51.6	54.8	56.5	37.0	54.6	43.6
Sm	7.75	8.69	7.43	8.38	9.51	9.81	11.4	7.77	10.66	8.83
Eu	2.30	2.57	2.13	2.43	2.53	2.50	3.31	2.57	3.19	2.64
Gd	6.70	7.42	6.34	7.16	7.88	7.98	10.0	7.21	9.13	7.99
Tb	0.96	1.05	0.88	1.01	1.12	1.13	1.40	1.07	1.28	1.16
Dy	5.19	5.74	4.78	5.56	6.14	6.12	7.75	6.02	7.04	6.56
Ho	0.98	1.06	0.91	1.04	1.15	1.14	1.44	1.17	1.32	1.27
Er	2.60	2.77	2.40	2.75	3.07	3.06	3.75	3.08	3.48	3.40
Tm	0.35	0.38	0.33	0.37	0.42	0.42	0.51	0.43	0.47	0.47
Yb	2.17	2.32	2.06	2.34	2.65	2.59	3.09	2.64	2.96	2.89
Lu	0.31	0.34	0.30	0.34	0.38	0.38	0.44	0.38	0.44	0.43
Hf	6.29	7.56	5.88	7.13	8.66	9.79	7.76	5.72	7.67	6.94
Ta	2.76	3.36	2.45	3.09	2.81	2.88	1.64	1.45	1.46	1.61
Pb	4.75	4.87	6.86	4.62	9.23	10.1	7.52	3.92	7.67	8.00
Th	3.12	3.10	2.85	3.23	3.38	3.48	2.27	2.18	2.45	3.88
U	0.78	1.27	0.67	0.84	0.83	0.86	0.64	0.58	0.61	1.03

Sample no.	GY14-43	GY14-02	GY14-03	GY14-12	GY14-30	GY14-32	GY14-34	GY14-35	GY14-36	GY14-02r
Rock type	Basalt	Ryolite	Ryolite	Ryolite	Ryolite	Ryolite	Ryolite	Ryolite	Ryolite	Ryolite
Major element (wt.%)										
SiO_2	51.70	75.33	75.29	74.40	74.60	75.20	75.00	73.50	75.50	
Al_2O_3	16.70	13.32	13.89	13.65	12.00	12.10	12.45	10.30	12.90	
Fe_2O_3	1.63	1.24	1.11	1.03	2.00	2.50	1.39	1.79	1.80	
FeO	6.73	0.09	0.10	0.15	0.54	0.34	0.47	0.15	0.13	
FeO^T	8.20	1.21	1.10	1.08	2.34	2.59	1.72	1.76	1.75	
CaO	6.37	0.91	0.88	0.96	0.28	0.22	0.63	2.08	0.56	
MgO	4.21	0.21	0.28	0.29	0.23	0.15	0.10	0.18	0.10	
K_2O	3.06	4.45	3.92	4.54	4.96	5.02	5.32	2.00	5.37	
Na_2O	3.72	4.03	4.22	4.47	3.47	3.71	3.26	1.60	3.22	
TiO_2	1.80	0.10	0.05	0.10	0.16	0.19	0.12	0.10	0.13	
P_2O_5	0.76	0.03	0.03	0.02	0.01	0.03	0.02	0.02	0.02	
MnO	0.11	0.02	0.03	0.03	0.01	0.01	0.01	0.03	0.01	
$Mol[(Na^+ + K^+)/Al^{3+}]$	0.57	0.86	0.81	0.90	0.92	0.95	0.89	0.47	0.86	
Trace element (ppm)										
Sc	18.8	1.78	1.70	0.72	1.00	1.42	2.21	1.80	1.93	1.85
Ti	14897	730	730	212	928	1264	772	546	702	734

(*continued on next page*)

Table 4 (*continued*)

V	202	3.3	1.1	3.4	7.6	10.9	13.2	1.7	5.0	3.1
Cr	8.40	1.01	0.97	1.10	1.50	2.11	1.78	2.11	1.35	1.05
Mn	883	93.7	155	214	65.0	102	50.5	171	46.5	95.2
Co	36.7	0.62	0.47	0.07	0.20	0.34	0.64	0.47	0.34	0.59
Ni	16.0	0.34	0.22	0.51	0.88	0.84	1.43	0.65	0.62	0.29
Rb	47.9	153	150	446	205	159	191	114	197	143
Sr	569	94.4	101	15.2	10.2	18.3	17.4	244.4	17.6	97.3
Y	31.5	13.7	15.0	34.9	38.5	17.2	40.1	29.3	35.3	13.3
Zr	276	139	144	160	495	445	294	217	263	140
Nb	27.5	13.0	13.7	83.9	69.6	55.5	41.4	30.1	38.1	13.4
Cs	0.92	2.86	3.17	5.90	2.87	2.21	2.93	35.5	3.22	2.97
Ba	712	554	533	49.8	10.4	173	100	224	112	557
La	40.5	51.4	53.8	16.8	65.4	156	118	88.9	126	51.0
Ce	84.1	88.9	91.9	46.0	102	99.6	196	142	191	88.8
Pr	10.4	8.80	9.31	5.29	16.1	32.6	23.7	17.8	24.8	8.79
Nd	42.8	28.5	29.5	21.8	54.7	112	80.7	61.4	85.5	28.0
Sm	8.52	4.22	4.37	6.95	9.9	14.7	12.6	9.8	13.1	4.14
Eu	2.59	0.60	0.63	0.02	0.15	0.37	0.59	0.44	0.60	0.62
Gd	7.90	2.93	3.11	7.28	7.43	8.19	9.30	7.38	9.36	2.89
Tb	1.14	0.44	0.48	1.23	1.24	0.97	1.38	1.07	1.35	0.44
Dy	6.38	2.51	2.68	7.08	7.71	4.69	7.65	5.79	7.38	2.46
Ho	1.23	0.50	0.53	1.35	1.62	0.82	1.49	1.09	1.39	0.48
Er	3.32	1.43	1.52	3.70	4.94	2.24	4.01	2.78	3.70	1.36
Tm	0.46	0.22	0.23	0.56	0.80	0.35	0.59	0.39	0.54	0.21
Yb	2.81	1.52	1.56	3.61	5.38	2.37	3.69	2.32	3.35	1.42
Lu	0.41	0.23	0.24	0.50	0.81	0.36	0.54	0.32	0.48	0.21
Hf	6.84	4.91	5.01	8.68	15.64	13.53	9.07	6.82	8.19	4.87
Ta	1.65	1.28	1.28	5.79	4.01	3.11	2.84	2.25	2.74	1.27
Pb	8.74	22.7	22.3	51.0	22.9	20.7	32.3	5.1	27.4	22.6
Th	3.93	13.5	13.6	31.6	18.6	16.8	18.6	14.4	18.5	13.3
U	1.05	2.27	2.81	2.93	2.56	1.96	2.41	2.30	2.12	2.32

shown), consistent with clinopyroxene and Fe-Ti oxides as the dominant liquidus minerals at this stage. Olivine crystallization is inferred to be absent at this stage due to the low MgO (1.84–4.21 wt%), low Ni contents (15.14–52.11 ppm) and especially no obvious evolution trend between MgO and Ni. Note that crustal contamination is inferred to be insignificant for these basaltic melts *en route to* the surface due to the absence of crustal contamination character of obvious negative Nb-Ta anomalies and negative relationships between Th/Nb (or U/Ta) and $\varepsilon_{Nd}(t)$ (or $\varepsilon_{Hf}(t)$) as previously discussed (Guo et al., 2014). In this case, the enrichment of K, Ba, and Pb in these mafic rocks (Fig. 5b) is inferred to be most probably inherited from the source region.

In general, the asthenosphere is distinct from the lithospheric mantle owing to their different rheology and history. The asthenospheric mantle is hot and convective and has a depleted incompatible element and isotopes compositions due to the circulation of incipient melts from low degrees partial melting. Thus, magmas derived from the asthenospheric mantle, e.g., the mid-ocean ridge basalts, are characterized by low $^{87}Sr/^{86}Sr$ and high ε_{Nd} and ε_{Hf} (Zindler and Hart, 1986). In contrast, the lithospheric mantle, taking the Mesozoic NCC as an example, is cold and isotopically enriched with high $^{87}Sr/^{86}Sr(t)$ and low $\varepsilon_{Nd}(t)$ and $\varepsilon_{Hf}(t)$ because of its low-F melt metasomatism history and long isolation from the convective mantle. In the case of mafic rocks from the Yinshan Block, they generally exhibit variably high $^{87}Sr/^{86}Sr(t)$ and low $\varepsilon_{Nd}(t)$ and $\varepsilon_{Hf}(t)$ relative to the primitive mantle (Fig. 6), with an obvious $\varepsilon_{Nd}(t)$-Sm/Nd trend (Fig. 8a), and rough $^{87}Sr/^{86}Sr(t)$-Rb/Sr (not shown) and $\varepsilon_{Hf}(t) - Lu/Hf$ (not shown) trends, consistent with the explanation that the isolated lithospheric mantle is ancient enough so as to accumulate radiogenic isotopes.

The mafic rocks are highly enriched with high $[La/Sm]_N = 2.75–3.73$ (with an average of 3.26 for $N = 11$), together with the more enriched character in the progressively more incompatible elements (Fig. 5b), suggesting that the source region had undergone a prior low mass fraction (low-F) melt enrichment or mantle metasomatism (Niu and O'Hara, 2003; Niu et al., 2012). The obvious positive correlation between $\varepsilon_{Nd}(t)$ and Sm/Nd (Fig. 8a), and negative correlation between $\varepsilon_{Nd}(t)$ and La/Sm further indicate the occurrence of ancient 'metasomatism', which is also consistent with the explanation by Tang et al. (2008). The highly varied initial Sr-Nd-Hf isotopic compositions here strongly indicate a long-time and complex metasomatism history of the lithospheric mantle. Note that the Th-U display striking trough in the primitive mantle normalized multi-element spidergram (Fig. 5b), which most probably results from contribution of metasomatic vein amphiboles because Nb-Ta-rich amphiboles in mantle peridotites have very conspicuous Th-U anomalies as shown in Fig. 5 (Ionov and Hofmann, 1995).

In summary, all the elemental and Sr-Nd-Hf isotope characteristics indicate that the basalts from the Yinshan Block were derived from partial melting of ancient metasomatized lithospheric mantle.

5.3. Petrogenesis of the rhyolites

Two main hypotheses have been proposed to explain the genesis of felsic end-member in bimodal magmatism (Niu et al., 2013): (1) A genetic relationship between mantle derived mafic and felsic rocks through fractional crystallization processes; (2) The felsic melts are generated either from the anatexis of crustal rocks or from partial melting of young underplated basalts.

Despite the similar emplacement age of the mafic and felsic volcanism, and the expected first order evolution trends from mafic to felsic in SiO_2 variation diagrams (Fig. 4), the obvious distinctions in Nd-Hf isotopic compositions (Fig. 6b) and ratios of element pairs with similar incompatibility (e.g., Nb/Th and Ta/U; Fig. 9) preclude the possibility of direct fractionation from mantle-derived mafic magmas to felsic magmas. Alternatively, these felsic rocks are highly enriched in incompatible elements, especially Nb-Ta for several samples (see Fig. 5d), inconsistent with the lower continental crust as the ultimate source. Thus, partial melting of the NCC lower crust alone also cannot explain the origin of these felsic rocks. In this case, hybridization between crustal anatectic granitic melts and mantle-derived mafic magmas is invoked here to account for the generation of magmas parental to the rhyolites (Figs. 5–6, and 9). A simple mixing calculation using Nd-Hf isotope is conducted here to evaluate the relative contribution of the crustal materials. In the calculation, we assume the average composition of basalts in this study as the mantle-origin-melt

Table 5
Bulk rock Sr–Nd–Hf isotope data analysis result on volcanic rocks from the Yinshan Block.

	$^{87}Rb/^{86}Sr$[a]	$^{87}Sr/^{86}Sr \pm 1SE$	$^{147}Sm/^{144}Nd$[a]	$^{143}Nd/^{144}Nd \pm 1SE$	$^{176}Lu/^{177}Hf$[a]	$^{176}Hf/^{177}Hf \pm 1SE$	$^{87}Sr/^{86}Sr_i$[b]	$^{143}Nd/^{144}Nd_i$[b]	$^{176}Hf/^{177}Hf_i$[b]	$\varepsilon_{Nd}(t)$[c]	$\varepsilon_{Hf}(t)$[c]
HQ14-01	0.335496542	0.706795 ± 10	0.113972	0.512139 ± 5	0.008567	0.282588 ± 6	0.706174	0.512042	0.282533	−9.74	−6.51
HQ14-04	0.455977081	0.706529 ± 7	0.113260	0.512179 ± 6	0.007586	0.282649 ± 5	0.705685	0.512083	0.282600	−8.96	−4.35
HQ14-05	0.651428255	0.709325 ± 8	0.113042	0.512127 ± 5	0.008880	0.282567 ± 6	0.708119	0.512031	0.282510	−9.97	−7.25
HQ14-08	0.373331301	0.706506 ± 8	0.112652	0.512163 ± 4	0.008215	0.282611 ± 4	0.705815	0.512067	0.282558	−9.27	−5.69
HQ14-12	0.37533225	0.707526 ± 7	0.110941	0.512033 ± 5	0.007479	0.282463 ± 5	0.706831	0.511939	0.282415	−11.80	−10.93
HQ14-17	0.157210237	0.708643 ± 7	0.109282	0.512016 ± 4	0.006859	0.282412 ± 5	0.708352	0.511923	0.282368	−12.14	−12.73
GY14-15	0.142566478	0.706630 ± 8	0.122211	0.512114 ± 5	0.010948	0.282509 ± 4	0.706366	0.512010	0.282438	−10.22	−9.30
GY14-17	0.129419646	0.705644 ± 8	0.127586	0.512391 ± 6	0.012680	0.282723 ± 6	0.705404	0.512282	0.282641	−4.82	−1.73
GY14-27	0.13717299	0.706787 ± 8	0.118291	0.512055 ± 4	0.010653	0.282423 ± 4	0.706533	0.511954	0.282354	−11.37	−12.35
GY14-39	0.241537064	0.706301 ± 8	0.123119	0.512173 ± 4	0.011401	0.282489 ± 5	0.705854	0.512068	0.282415	−9.07	−10.01
GY14-43	0.259106884	0.706329 ± 6	0.122218	0.512142 ± 5	0.011302	0.282474 ± 5	0.705849	0.512038	0.282401	−9.68	−10.54
GY14-02	4.605492447	0.715860 ± 9	0.089774	0.511761 ± 4	0.007637	0.282246 ± 4	0.707335	0.511685	0.282197	−17.11	−18.60
GY14-03	48.23160182	0.715976 ± 9	0.190608	0.511751 ± 6	0.010091	0.282243 ± 5	0.626694	0.511589	0.282178	−17.31	−18.71
GY14-12	4.436722802	0.789210 ± 14	0.089087	0.512024 ± 7	0.007982	0.282399 ± 5	0.780997	0.511948	0.282347	−11.98	−13.19
GY14-30	49.24545473	0.792005 ± 30	0.107238	0.511982 ± 5	0.007845	0.282354 ± 5	0.700846	0.511891	0.282303	−12.80	−14.78
GY14-32	24.13052362	0.746863 ± 22	0.080427	0.511951 ± 4	0.004235	0.282342 ± 4	0.702195	0.511883	0.282315	−13.40	−15.21
GY14-34	31.15743101	0.763716 ± 9	0.093984	0.51196 ± 4	0.009989	0.282344 ± 4	0.706040	0.511880	0.282279	−13.23	−15.14
GY14-35	1.52194777	0.712608 ± 10	0.096302	0.511962 ± 5	0.008644	0.282342 ± 5	0.709791	0.511880	0.282286	−13.19	−15.21
GY14-36	28.13710113	0.763586 ± 19	0.093053	0.511956 ± 4	0.011874	0.282355 ± 4	0.711501	0.511877	0.282278	−13.31	−14.75
HQ14-17R	0.157210237	0.708680 ± 5	0.109282	0.512011 ± 4	0.006859	0.282409 ± 4	0.708389	0.511918	0.282365	−12.23	−12.84
BHVO-2		0.703474 ± 8		0.512954 ± 5		0.283089 ± 4					

[a] $^{87}Rb/^{86}Sr$, $^{147}Sm/^{144}Nd$ and $^{176}Lu/^{177}Hf$ are calculated using whole-rock Rb, Sr, Sm, Nd, Lu and Hf contents in Table 4.
[b] $^{87}Sr/^{86}Sr_i = [(^{87}Sr/^{86}Sr) - (^{87}Rb/^{86}Sr)(e^{\lambda t} - 1)]$; $^{143}Nd/^{144}Nd_i = [(^{143}Nd/^{144}Nd) - (^{143}Sm/^{144}Nd)(e^{\lambda t} - 1)]$; $^{176}Hf/^{177}Hf_i = [(^{176}Hf/^{177}Hf) - (^{176}Lu/^{177}Hf)(e^{\lambda t} - 1)]$.
[c] $\varepsilon Nd(t) = [(^{143}Nd/^{144}Nd_i)/(^{143}Nd/^{144}Nd_{CHURi}) - 1] \times 10{,}000$, $^{143}Nd/^{144}Nd_{CHUR} = 0.512638$; $\varepsilon_{Hf}(t) = [(^{176}Hf/^{177}Hf_i)/(^{176}Hf/^{177}Hf_{CHURi}) - 1] \times 10{,}000$; $^{176}Hf/^{177}Hf_{CHUR} = 0.282772$.

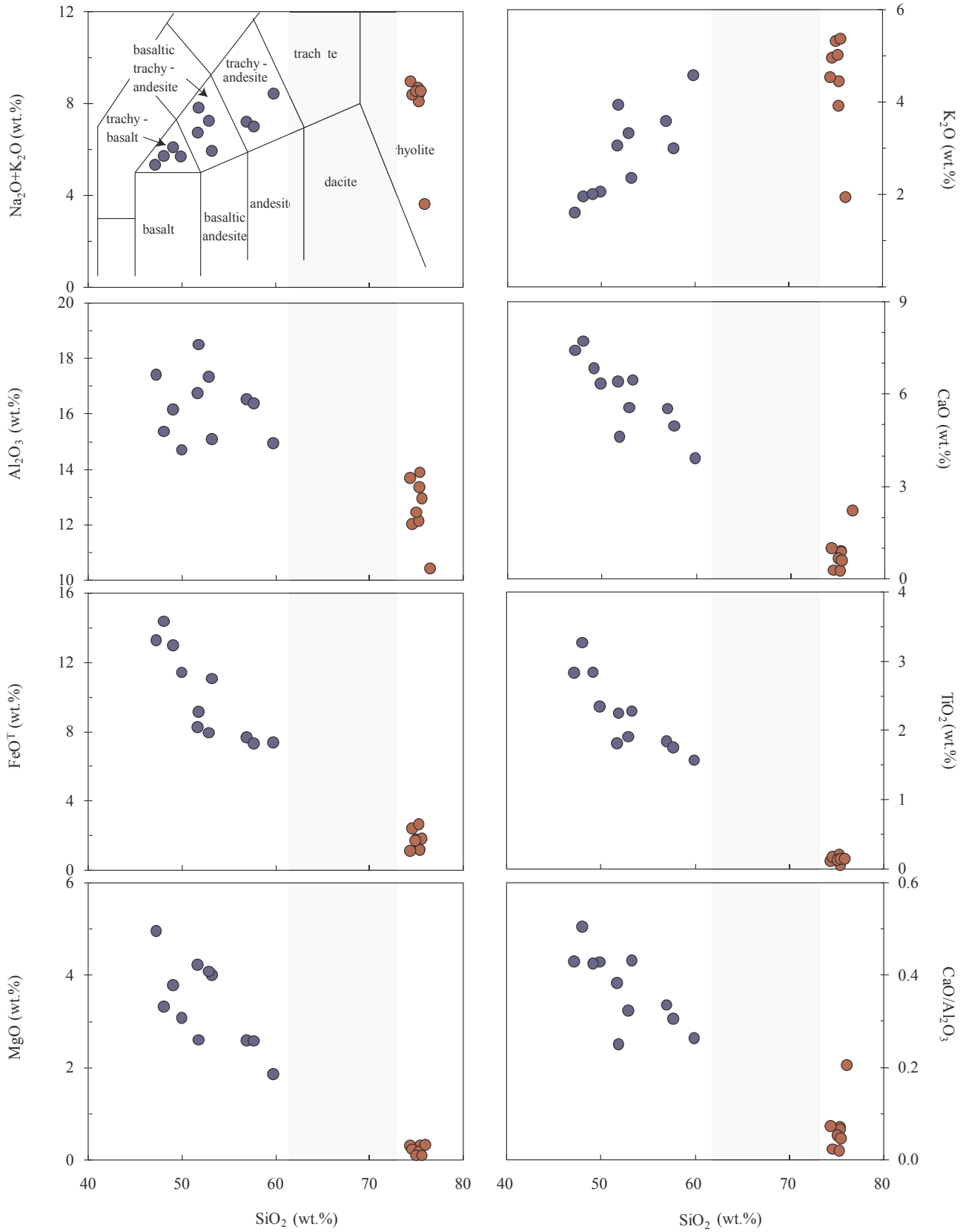

Fig. 4. SiO_2-variation diagrams, including alkaline (K_2O + Na_2O), major element oxides and CaO/Al_2O_3, to show the bimodal affinity of Early Cretaceous volcanic rocks from Yinshan Block. Blue solid circles indicate mafic samples and red solid circles indicate felsic samples. All the data plotted in the K_2O + Na_2O vs. SiO_2 diagram (Le Bas et al., 1986) have been normalized to 100% on a volatile-free basis.

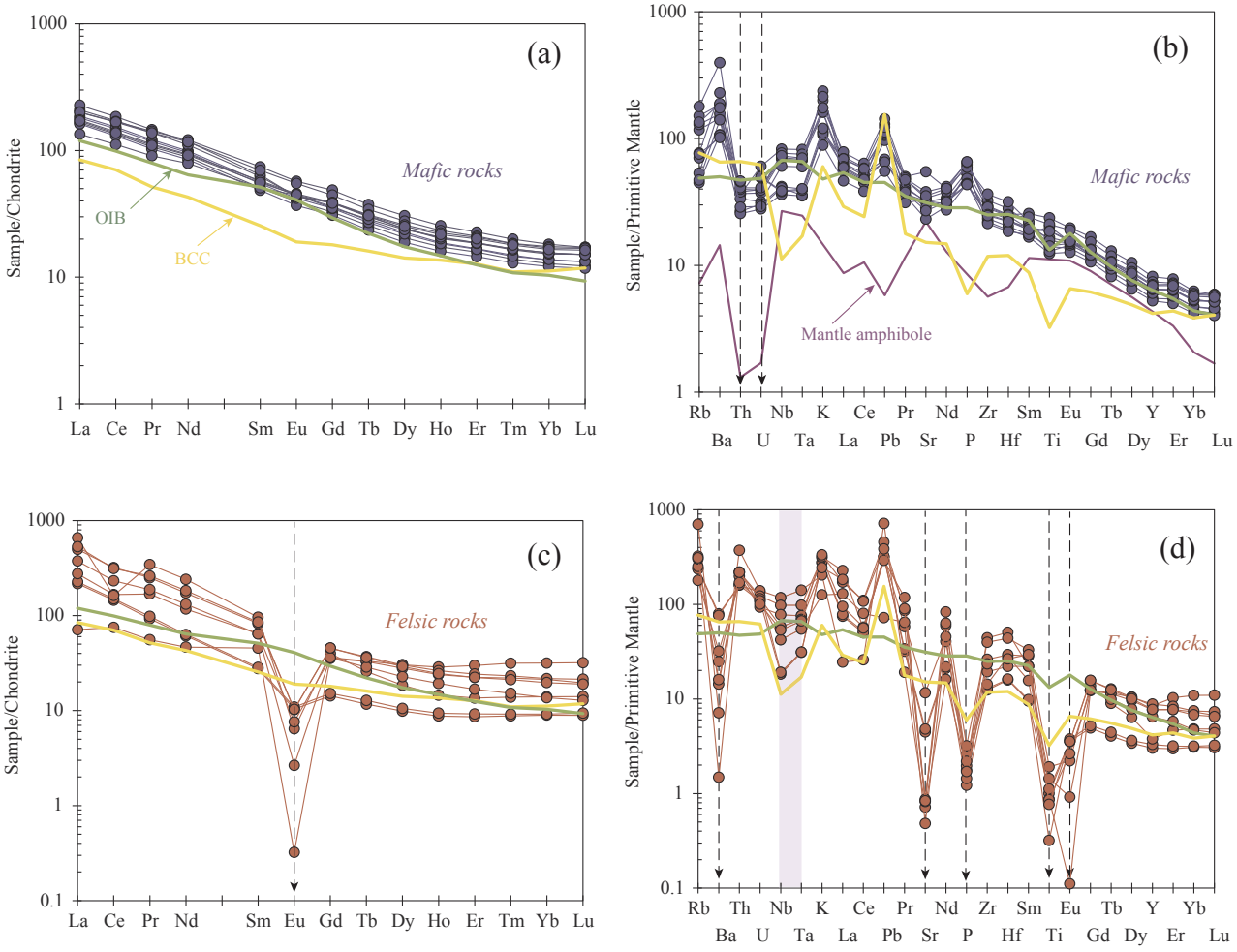

Fig. 5. (a, c) Chondrite normalized rare earth element patterns and (b, d) primitive mantle normalized incompatible element patterns of Early Cretaceous volcanic rocks from Yinshan Block. Chondrite and primitive mantle values are from Sun and McDonough (1989). For comparison, average present-day ocean island basalts (OIBs) (Sun and McDonough, 1989) and the average NCC crust (Gao et al., 1998b) are plotted. We also plot the mantle amphibole data (Ionov and Hofmann, 1995) on the diagram (b) to illustrate the potential mantle amphibole contributions to the source region of the mafic rocks.

end-member. For easy understanding in concept, the sample GY14-02 with the most negative Nb-Ta anomalies is assumed here to be the crust-origin-melt end-member, despite the lower crust of the NCC is highly heterogeneous (Jiang et al., 2013). The result indicates that ~35–60% mantle-derived alkaline basaltic melts and ~40–65% crustal anatectic granitic melts have been involved to produce the observed geochemical composition of the rhyolites (Fig. 8b).

However, the mixing between mantle-derived alkaline basaltic melts (< 52 w.t.% SiO_2) and crustal anatectic granitic melts (> 65 w.t.% SiO_2) would generate andesitic melts with SiO_2 < 65 w.t.%, which is inconsistent with the observed rhyolites composition with SiO_2 > 65 w.t.%, very low Cr (0.97–2.11 ppm) and Ni (0.22–1.43 ppm) (Table 2). In this case, the mixed magmas must have experienced high degree of fractional crystallization. The low Cr and Ni here might be related to the fractionation of clinopyroxene at the earlier stage. The significant Ba-Sr-Eu troughs on the multi-element spidergram (Fig. 5d) in rhyolites is a straightforward consequence of plagioclase-dominated fractionation, because plagioclase is the only known phase that can simultaneously and effectively fractionate Ba, Eu and Sr from other elements ($Kd_{Sr} \gg 1$, $Kd_{Eu} \gg 1$, $Kd_{Ba} \gg 1$; Niu and O'Hara,

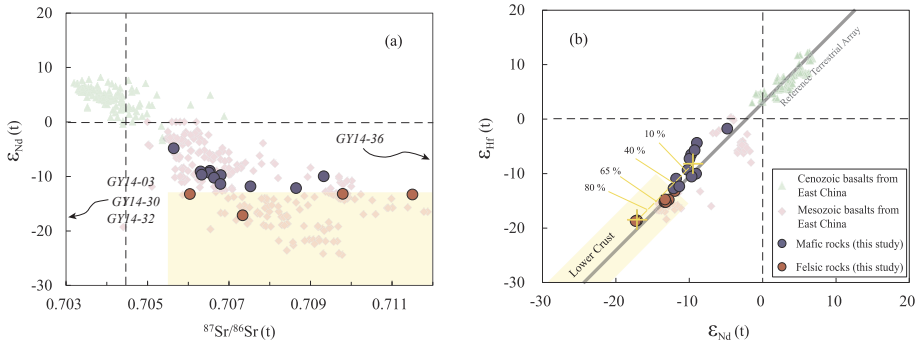

Fig. 6. Sr, Nd and Hf isotope compositions of the Early Cretaceous volcanic rocks from Yinshan Block. Also shown are the published Sr–Nd-Hf isotope data of Cenozoic basalts and Mesozoic basalts from Eastern China (Zhang et al., 2002, 2003; Fan et al., 2001; Liu et al., 2008; Gao et al., 1998a,b; Yang and Li, 2008; Ling et al., 2009; Tang et al., 2013; Liu et al., 2014; Zhou et al., 2015; Meng et al., 2015; Guo et al., 2016). Reference Terrestrial Array ($\varepsilon_{Hf} = 1.36\varepsilon_{Nd} + 2.95$) is after Vervoort and Blichert-Toft (1999). The lower crust region is from Jiang et al. (2013). A simple mixing between mantle-derived alkaline basaltic melts and crustal anatectic granitic melts have been calculated using Nd-Hf isotope. The assumed basaltic end-member is our averaged mafic samples (Nd = 46.62 ppm, Hf = 7.29 ppm, $\varepsilon_{Nd}(t) = -9.73$, $\varepsilon_{Hf}(t) = -8.31$), while the felsic end-member is assumed using the Nb-Ta most depleted sample GY14-02 (Nd = 28.48 ppm, Hf = 4.91 ppm, $\varepsilon_{Nd}(t) = -17.11$, $\varepsilon_{Hf}(t) = -18.6$).

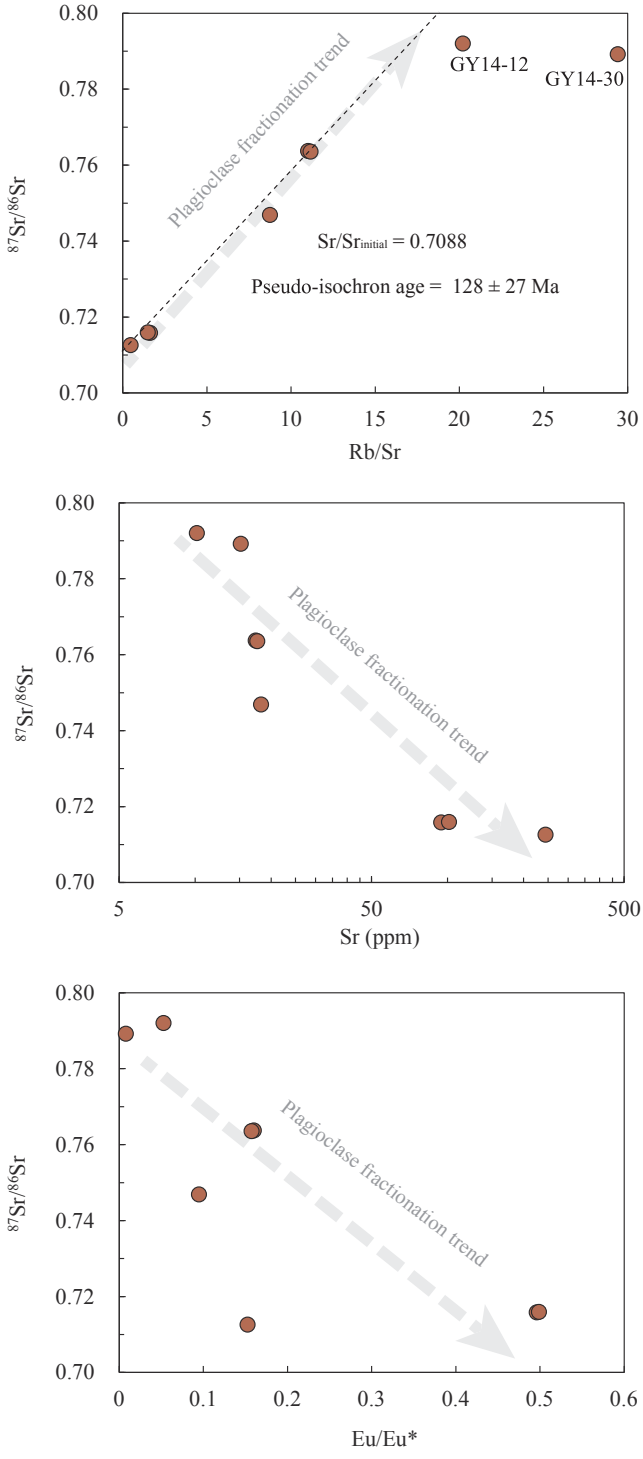

Fig. 7. $^{87}Sr/^{86}Sr$ vs. Rb/Sr, $^{87}Sr/^{86}Sr$ vs. Sr and $^{87}Sr/^{86}Sr$ vs. Eu/Eu^* diagrams to illustrate that protracted fractional crystallization of plagioclase (K-rich feldspars in highly evolved rhyolites) controlled the observed compositional variations of rhyolitic rocks. Note that Rb–Sr isotope pseudochron age (128 ± 27 Ma) is defined by most of the analyzed felsic samples (except for sample GY14-12 and GY14-30).

2009). Furthermore, crystallization of K-feldspar at the trachytic stage and thereafter will strengthen these Ba, Eu and Sr depleted characteristics (Shao et al., 2015). Fig. 7 further illustrates this concept with the positive correlation between $^{87}Sr/^{86}Sr$ and Rb/Sr (with an isochron age of 128 ± 27 Ma), negative correlation between $^{87}Sr/^{86}Sr$ and Sr, $^{87}Sr/^{86}Sr$ and Eu/Eu^*. Because plagioclase (to a lesser extent K-feldspar also) crystallization depletes Sr, Eu, while raises Rb/Sr ratio in the

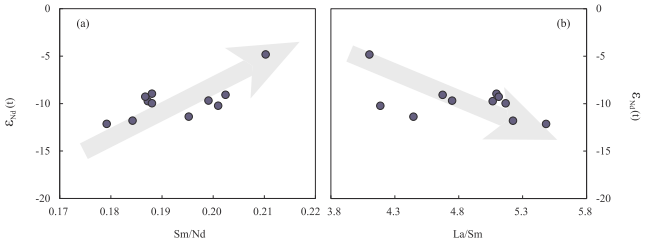

Fig. 8. $^{143}Nd/^{144}Nd$ against Sm/Nd and La/Sm to illustrate that radiogenic isotopes of mafic rocks are supported by parent/daughter ratios, suggesting ancient source enrichment.

residual melts, thus the highly evolved rhyolites should have extremely low Sr content at the time of felsic magma solidification, and the present-day measured Sr in these rocks are expected mostly radiogenic ^{87}Sr. This explains the 'unexpectedly' high $^{87}Sr/^{86}Sr$ ratios in the highly evolved rhyolites in this study.

5.4. Implication for reworking of lower continental crust of the North China Craton

The Early Cretaceous volcanism is widespread in East China as studied by many (Zhang et al., 2002, 2003; Fan et al., 2001; Liu et al., 2008; Gao et al., 1998a,b; Yang and Li, 2008; Xu et al., 2008, 2013; Ling et al., 2009; Tang et al., 2013; Liu et al., 2014; Zhou et al., 2015). The Mesozoic bimodal volcanic rocks have also been reported in East China, for example in the Hainan Island and Jiaozhou basin (Fan et al., 2001; Ling et al., 2009; Zhou et al., 2015). The close spatial and temporal association of these Early Cretaceous volcanism is the convincing evidence that they are results of the lithosphere thinning (Niu, 2005, 2014). What we emphasize here is that our petrogenetic model of these volcanic rocks from the Yinshan Block might be of general significance for all the early Cretaceous bimodal suites in eastern China, in which basaltic magmatism resulted from partial melting of lithospheric mantle, while the felsic rocks were produced through continental crust anatexis induced by the underplating basaltic magma (see Niu et al., 2015). Such a model better explains the origin of the 'Daly Gap' in those alkaline volcanic rocks in an intra-plate setting.

Because the felsic magmatism is widespread as well as the basaltic volcanism, and because the felsic magmatism is considered as the result of anatexis at crustal levels (see above), we thus propose that the extraction of these felsic melts from the crustal source region is a possible process that thinned the deep crust of East China. Apart from the felsic volcanism mentioned above, the observation that the large scale of Yanshanian granitoids distributed in NE-SW direction is also the evidence that the anatexis at crustal levels occurred widespread throughout East China (Niu et al., 2015).

We use a cartoon to illustrate the petrogenesis of the bimodal volcanism in the Yinshan Block (Fig. 10). The basaltic magmas were produced by partial melting of ancient metasomatized mantle lithosphere through basal hydration, in which the water released from the stagnant Paleo-Pacific slab (see Niu, 2005, 2014 for details). These basaltic magmas migrated upward and erupted onto the surface, and the mafic rocks from the Yinshan Block represent evolved magmas derived from metasomatized ancient lithospheric mantle. However, with large scale of basaltic magma underplating, anatexis at the crustal level would be inevitable. The underplating basaltic magma not only provided the heat for the anatexis, but also contributed materials. The subsequent plagioclase (also K-feldspar to a less extent) crystallization resulted in the depletion of Ba, Sr, Eu, and thus extremely radiogenic $^{87}Sr/^{86}Sr$ in the felsic magmas.

6. Conclusions

(1) The Ar-Ar dating of the early Cretaceous basaltic rocks from the

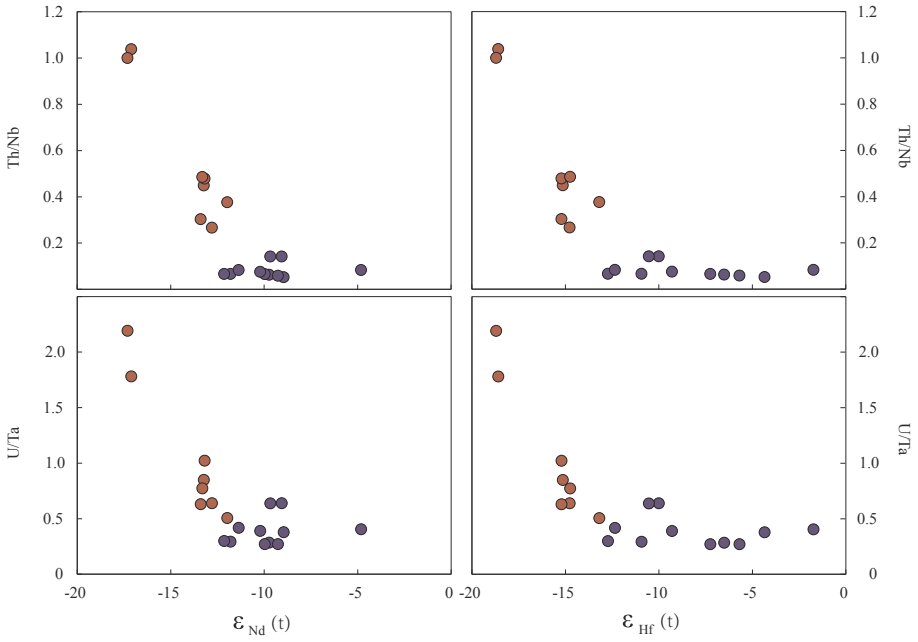

Fig. 9. Th/Nb and U/Ta against ε_{Nd} and ε_{Hf} diagrams to illustrate that the felsic rocks and mafic rocks were originated from different source region.

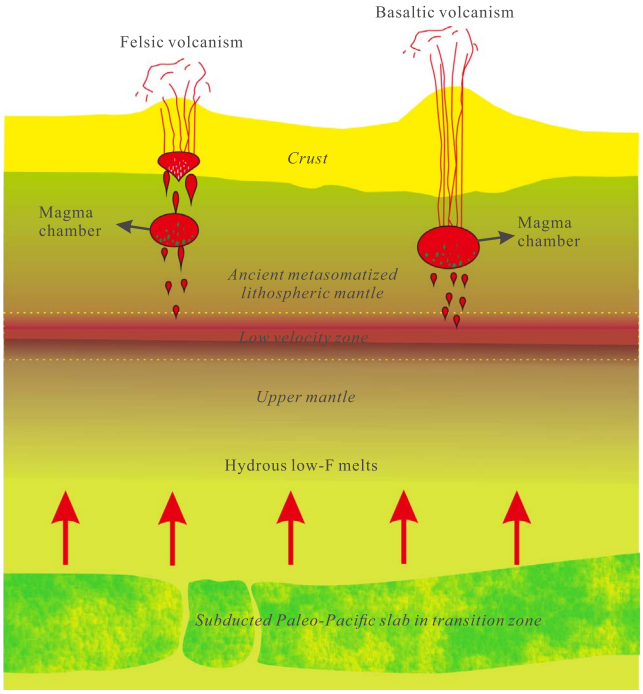

Fig. 10. Graphical description of the petrogenesis of Early Cretaceous volcanic rocks from Yinshan Block. Partial melting of an ancient metasomatized lithosphere mantle through basal hydration produced alkaline magmas in Yinshan Block, while anatexis at the crustal level induced by underplated basaltic magmas produced felsic magmas. The protracted plagioclase (also K-feldspar to less extent) crystallization results in the observed depletion of Ba, Sr, Eu, and thus very high $^{87}Sr/^{86}Sr$.

Yinshan Block gives eruption ages of 107–133 Ma, while the zircon SHIRMP U-Pb dating of the rhyolites gives an emplacement age of ~126 Ma.

(2) Magmas parental to the basaltic rocks were originated from partial melting of ancient metasomatized sub-continental lithospheric mantle, whereas melts parental to the rhyolites were produced by mixing of mantle-derived alkaline mafic melts and lower crust anatexis derived felsic melts.

(3) Protracted plagioclase crystallization played dominant roles during the evolution of the rhyolitic melts, which depletes Ba, Sr and Eu in the residual melts with diminishing Eu/Eu* values. The very high Rb/Sr ratio explains the extremely radiogenic Sr isotopes in the rhyolitic rocks, giving a significant isochron age.

(4) The occurrence of the early Cretaceous bimodal magmatism in the Yinshan Block confirms our previous proposal that the lithosphere beneath western NCC had also been thinned.

(5) Basaltic magmas underplating caused the lower crust anatexis, resulting in lower crust thinning in East China. This model is of general significance for the destruction of the NCC.

Acknowledgments

We are grateful to H.N. Qiu, X.J. Bai and X.C. Che for their assistance with bulk rock Ar-Ar dating on basalts and zircon SHRIMP U-Pb dating on rhyolites, respectively. The authors wish to thank T.P. Zhao for handling the manuscript and Y.J. Tang and W.L. Xu for their helpful advice on the manuscript. This work was jointly supported by the National Natural Science Foundation of China – China (NSFC grants 41630968, 91014003 and 41130314), Chinese Academy of Sciences (Innovation grant Y42217101L), and the Knowledge Innovation Program of the Sanya Institute of Deep-sea Science and Engineering, Chinese Academy of Sciences (Grant Y570031QY1).

References

Aydin, F., Schmitt, A.K., Siebel, W., Duncan, R., 2014. Quaternary bimodal volcanism in the Niğde Volcanic Complex (Cappadocia, central Anatolia, Turkey): age, petrogenesis and geodynamic implications. Contrib. Miner. Petrol. 168, 1–24.

Black, L.P., Kamo, S.L., Allen, C.M., Aleinikoff, J.N., Davis, D.W., Korsch, R.J., Foudoulis, C., 2003. TEMORA 1: a new zircon standard for phanerozoic U-Pb geochronology. Chem. Geol. 200, 155–170.

Bonnefoi, C.C., Provost, A., Alberade, F., 1995. The 'Daly gap' as a magmatic catastrophe. Nature 378, 270–272.

Cann, J.R., 1968. Bimodal distribution of rocks fromvolcanic islands. Earth Planet. Sci. Lett. 4, 479–480.

Carlson, R.W., Pearson, D.G., James, D.E., 2005. Physical, chemical, and chronological characteristics of continental mantle. Rev. Geophys. 43, RG1001.

Chayes, F., 1963. Relative abundance of intermediate members of the oceanic basalt—trachyte association. J. Geophys. Res. 68, 1519–1534.

Chen, S., Wang, X.H., Niu, Y.L., Ellipsis Xue, Q.Q., 2017. Simple and cost-effective methods for precise analysis of trace element abundances in geological materials with ICP-MS. Sci. Bull. 62, 277–289.

Chen, Z.G., Zhang, L.C., Wu, Y.H., Zhou, X.H., Liu, Q., 2009. Ar-Ar age, geochemistry and petrogenesis of late Mesozoic volcanic rocks in the northern marginal region of Erlian

basin, Inner-Mongolia. Acta Petrol. Sin. 25, 297–310 (in Chinese with English abstract).
Clague, D.A., 1978. The oceanic basalt-trachyte association: an explanation of the Daly gap. J. Geol. 739–743.
Fan, W.M., Guo, F., Wang, Y.J., Lin, G., Zhang, M., 2001. Post-orogenic bimodal volcanism along the Sulu orogenic belt in eastern China. Phys. Chem. Earth (A) 26, 733–746.
Fan, W.M., Zhang, H.F., Baker, J., Jarvis, K.E., Mason, P.R.D., Menzies, M.A., 2000. On and off the North China Craton: where is the Archaean Keel? J. Petrol. 41, 933–950.
Ferla, P., Meli, C., 2006. Evidence of magma mixing in the 'Daly Gap' of alkaline suites: a case study from the enclaves of Pantelleria (Italy). J. Petrol. 47, 1467–1507.
Gao, S., Luo, T.C., Zhang, B.R., Zhang, H.F., Han, Y.W., Zhao, Z.D., Hu, Y.K., 1998b. Chemical composition of the continental crust as revealed by studies in East China. Geochim. Cosmochim. Acta 62, 1959–1975.
Gao, S., Rudnick, R.L., Carlson, R.W., McDonough, W.F., Liu, Y.S., 2002. Re–Os evidence for replacement of ancient mantle lithosphere beneath the North China craton. Earth Planet. Sci. Lett. 198, 307–322.
Gao, S., Rudnick, R.L., Yuan, H.L., Liu, X.M., Liu, Y.S., Xu, W.L., Ling, W.L., Ayers, J., Wang, X.C., Wang, Q.H., 2004. Recycling lower continental crust in the North China craton. Nature 432, 892–897.
Gao, S., Zhang, B.R., Jin, Z.M., Kern, H., Luo, T.C., Zhao, Z.D., 1998a. How mafic is the lower continental crust? Earth Planet. Sci. Lett. 161, 101–117.
Griffin, W.L., Zhang, A., O'Reilly, S.Y., Ryan, C.G., 1998. Phanerozoic evolution of the lithosphere beneath the Sino-Korean craton. In: Flower, M.F.J., Chung, S.-L., Lo, C.-H., Lee, T.-Y. (Eds.), Mantle Dynamics and Plate Interactions in East Asia: Geodynamics Series. American Geophysical Union, pp. 107–126.
Guo, P.Y., Niu, Y.L., Ye, L., Liu, J.J., Sun, P., Cui, H.X., Su, L., Zhao, J.X., Feng, Y.X., 2014. Lithosphere thinning beneath west North China Craton: evidence from geochemical and Sr–Nd–Hf isotope compositions of Jining basalts. Lithos 202, 37–54.
Guo, P.Y., Niu, Y.L., Sun, P., Ye, L., Liu, J.J., Zhang, Y., Feng, Y.X., Zhao, J.X., 2016. The origin of Cenozoic basalts from central Inner Mongolia, East China: the consequence of recent mantle metasomatism genetically associated with seismically observed paleo-Pacific slab in the mantle transition zone. Lithos 240, 104–118.
He, Y.K., Wu, T.R., Jing, X., 2013. $^{40}Ar/^{39}Ar$ laser probe dating of Siziwangqi shoshonite and its geological significance. Geol. Explor. 49, 1114–1122 (in Chinese with English abstract).
Ionov, D.A., Hofmann, A.W., 1995. Nb-Ta-rich mantle amphiboles and micas: Implications for subduction-related metasomatic trace element fractionations. Earth Planet. Sci. Lett. 131, 341–356.
Jiang, N., Guo, J., Chang, G., 2013. Nature and evolution of the lower crust in the eastern North China craton: a review. Earth-Sci. Rev. 122, 1–9.
Koppers, A.A.P., 2002. ArArCALC—software for $^{40}Ar/^{39}Ar$ age calculations. Comput. Geosci. 28, 605–619.
Lacasse, C., Sigurdsson, H., Carey, S.N., Jóhannesson, H., Thomas, L.E., Rogers, N.W., 2007. Bimodal volcanism at the Katla subglacial caldera, Iceland: insight into the geochemistry and petrogenesis of rhyolitic magmas. Bull. Volcanol. 69, 373–399.
Le Bas, M.J., Le Maître, R.W., Streckeisen, A., Zanettin, B., 1986. A chemical classification of volcanic rocks based on the total-alkali silica (TAS) diagram. J. Petrol. 27, 745–750.
Li, S., Mooney, W.D., 1998. Crustal structure of China from deep seismic sounding profiles. Tectonophysics 288, 105–113.
Li, S., Mooney, W.D., Fan, J., 2006a. Crustal structure of mainland China from deep seismic sounding data. Tectonophysics 420, 239–252.
Li, X.H., Li, Z.X., Wingate, M.T.D., Chung, S.L., Liu, Y., Lin, G.C., Li, W.X., 2006b. Geochemistry of the 755 Ma Mundine Well dyke swarm, northwestern Australia: part of a Neoproterozoic mantle superplume beneath Rodinia? Precambrian Res. 146, 1–15.
Ling, W.L., Duan, R.C., Xie, X.J., Zhang, Y.Q., Zhang, J.B., Cheng, J.P., Yang, H.M., 2009. Contrasting geochemistry of the Cretaceous volcanic suites in Shandong province and its implications for the Mesozoic lower crust delamination in the eastern North China craton. Lithos 113, 640–658.
Liu, J.J., Ye, L., Niu, Y.L., Guo, P.Y., Sun, P., Cui, H.X., 2014. The geochemistry of late Mesozoic volcanic rocks from the North China Craton and temporal and spatial constraints on the lithospheric thinning. Geol. J. China Univ. 20, 491–506 (in Chinese with English abstract).
Liu, P.P., Zhou, M.F., Ren, Z., Wang, C.Y., Wang, K., 2016. Immiscible Fe- and Si-rich silicate melts in plagioclase from the Baima mafic intrusion (SW China): implications for the origin of bi-modal igneous suites in large igneous provinces. J. Asian Earth Sci. 127, 211–230.
Liu, Y.S., Gao, S., Kelemen, P.B., Xu, W.L., 2008. Recycled crust controls contrasting source compositions of Mesozoic and Cenozoic basalts in the North China Craton. Geochim. Cosmochim. Acta 72, 2349–2376.
Marzoli, A., Renne, P.R., Piccirillo, E.M., Ellipsis N'ni, J., 1999. Silicic magmas from the continental Cameroon Volcanic Line (Oku, Bambouto and Ngaoundere): ^{40}Ar-^{39}Ar dates, petrology, Sr-Nd-O isotopes and their petrogenetic significance. Contrib. Miner. Petrol. 135, 133–150.
Mazzarini, F., Corti, G., Manetti, P., Innocenti, F., 2004. Strain rate and bimodal volcanism in the continental rift: Debre Zeyt volcanic field, northern MER, Ethiopia. J. Afr. Earth Sci. 39, 415–420.
Meng, F., Gao, S., Niu, Y., Liu, Y., Wang, X., 2015. Mesozoic-Cenozoic mantle evolution beneath the North China Craton: a new perspective from Hf–Nd isotopes of basalts. Gondwana Res. 27, 1574–1585.
Menzies, M.A., Fan, W., Zhang, M., 1993. Palaeozoic and Cenozoic lithoprobes and the loss of N120 km of Archaean lithosphere, Sino-Korean craton, China. In: Prichard, H. M., et al. (Eds.), Magmatic Processes and Plate Tectonics, Geol. Soc. Spec. Publ., vol. 76, pp. 71–81.
Niu, Y.L., 2005. Generation and evolution of basaltic magmas: some basic concepts and a hypothesis for the origin of the Mesozoic and Cenozoic volcanism in eastern China. Geol. J. China Univ. 11, 9–46.
Niu, Y.L., 2014. Geological understanding of plate tectonics: basic concepts, illustrations, examples and new perspectives. Global Tecton. Metallog. 10, 23–46.
Niu, Y.L., Liu, Y., Xue, Q.Q., Ellipsis Zhang, Y., 2015. Exotic origin of the Chinese continental shelf: new insights into the tectonic evolution of the western Pacific and eastern China since the Mesozoic. Sci. Bull. 60, 1598–1616.
Niu, Y.L., O'Hara, M.J., 2003. Origin of ocean island basalts: a new perspective from petrology, geochemistry, and mineral physics considerations. J. Geophys. Res. 108 (B4), 2209.
Niu, Y.L., O'Hara, M.J., 2009. MORB mantle hosts the missing Eu (Sr, Nb, Ta and Ti) in the continental crust: new perspectives on crustal growth, crust–mantle differentiation and chemical structure of oceanic upper mantle. Lithos 112, 1–17.
Niu, Y.L., Wilson, M., Humphreys, E.R., O'Hara, M.J., 2012. A trace element perspective on the source of ocean island basalts (OIB) and fate of subducted oceanic crust (SOC) and mantle lithosphere (SML). Episodes 35, 310–327.
Niu, Y.L., Zhao, Z.D., Zhu, D.C., Mo, X.X., 2013. Continental collision zones are primary sites for net continental crust growth – a testable hypothesis. Earth-Sci. Rev. 127, 96–110.
Peccerillo, A., Barberio, M.R., Yirgu, G., Ayalew, D., Barbieri, M., Wu, T.W., 2003. Relationship between mafic and peralkaline felsic magmatism in continental rift settings: a petrological, geochemical and isotopic study of the Gedemsa Volcano, Central Ethiopian Rift. J. Petrol. 44, 2003–2032.
Peccerillo, A., Donati, C., Santo, A.P., Orlando, A., Yirgu, G., Ayalew, D., 2007. Petrogenesis of silicic peralkaline rocks in the Ethiopian rift: geochemical evidence and volcanological implications. J. Afr. Earth Sci. 48, 161–173.
Petrinovic, I.A., Riller, U., Brod, J.A., Alvarado, G., Arnosio, M., 2006. Bimodal volcanism in a tectonic transfer zone: evidence for tectonically controlled magmatism in the southern Central Andes, NW Argentina. J. Volcanol. Geotherm. Res. 152, 240–252.
Qiu, H.N., Bai, X.J., Liu, W.G., Mei, L.F., 2015. Automatic $^{40}Ar/^{39}Ar$ dating technique using multicollector ArgusVI MS with home-made apparatus. Geochimica 44, 477–484.
Shao, F.L., Niu, Y.L., Regelous, M., Zhu, D.C., 2015. Petrogenesis of peralkaline rhyolites in an intra-plate setting: Glass House Mountains, southeast Queensland, Australia. Lithos 216, 196–210.
Shellnutt, J.G., Zhou, M.F., Zellmer, G.F., 2009. The role of Fe–Ti oxide crystallization in the formation of A-type granitoids with implications for the Daly gap: an example from the Permian Baima igneous complex, SW China. Chem. Geol. 259, 204–217.
Shinjo, R., Kato, Y., 2000. Geochemical constraints on the origin of bimodal magmatism at the Okinawa Trough, an incipient back-arc basin. Lithos 54, 117–137.
Sun, S.S., McDonough, W.F., 1989. Chemical and isotopic systematics of ocean basalt: implications for mantle composition and processes. Geol. Soc. Lond. 42, 323–345 Special Publications.
Tang, Y.J., Zhang, H.F., Ying, J.F., Zhang, J., Liu, X.M., 2008. Refertilization of ancient lithospheric mantle beneath the central North China Craton: evidence from petrology and geochemistry of peridotite xenoliths. Lithos 101, 435–452.
Tang, Y.J., Zhang, H.F., Ying, J.F., Su, B.X., Li, X.H., Santosh, M., 2013. Rapid eruption of the Ningwu volcanics in eastern China: response to Cretaceous subduction of the Pacific plate. Geochem. Geophys. Geosyst. 14, 1703–1721.
Van Wagoner, N.A., Leybourne, M.I., Dadd, K.A., Baldwin, D.K., McNeil, W., 2002. Late Silurian bimodal volcanism of southwestern New Brunswick, Canada: products of continental extension. Geol. Soc. Am. Bull. 114, 400–418.
Vervoort, J.D., Blichert-Toft, J., 1999. Evolution of the depleted mantle: Hf isotope evidence from juvenile rocks through time. Geochim. Cosmochim. Acta 63, 533–556.
Williams, I.S., 1998. U-Th–Pb geochronology by ion microprobe. In: In: McKibben, M.A., Shanks, W.C., Ridley, W.I. (Eds.), Applications of Microanalytical Techniques to Understanding Mineralizing Processes, vol. 7. Reviews in Economic Geology, pp. 1–35.
Xu, C., He, Y.K., Wu, T.R., Zheng, R.G., Zhang, W., Meng, Q.P., Zhang, Z.Y., 2014. Geochemical characteristics of early cretaceous shoshonites in the Middle and Western Northern Margin of the North China Craton and a comparative study. Acta Sci. Nat. Univ. Pekinensis 50, 305–315 (in Chinese with English abstract).
Xu, W.L., Pei, F.P., Wang, F., Meng, E., Ji, W.Q., Yang, D.B., Wang, W., 2013. Spatial–temporal relationships of Mesozoic volcanic rocks in NE China: constraints on tectonic overprinting and transformations between multiple tectonic regimes. J. Asian Earth Sci. 74, 167–193.
Xu, W.L., Hergt, J.M., Gao, S., Pei, F.P., Wang, W., Yang, D.B., 2008. Interaction of adakitic melt-peridotite: implications for the high-$Mg^{\#}$ signature of Mesozoic adakitic rocks in the eastern North China Craton. Earth Planet. Sci. Lett. 265, 123–137.
Xu, Y.G., 2001. Thermo-tectonic destruction of the Archaean lithospheric keel beneath the Sino-Korean craton in China: evidence, timing and mechanism. Phys. Chem. Earth (A) 26, 747–757.
Yang, W., Li, S.G., 2008. Geochronology and geochemistry of the Mesozoic volcanic rocks in Western Liaoning: implications for lithospheric thinning of the North China Craton. Lithos 102, 88–117.
Zhang, H.F., Sun, M., Zhou, X.H., Fan, W.M., Zhai, M.G., Yin, J.F., 2002. Mesozoic lithosphere destruction beneath the North China Craton: evidence from major-, trace-element and Sr–Nd–Pb isotope studies of Fangcheng basalts. Contrib. Mineral. Petrol. 144, 241–254.
Zhang, H.F., Sun, M., Zhou, X.H., Zhou, M.F., Fan, W.M., Zheng, J.P., 2003. Secular evolution of the lithosphere beneath the eastern North China Craton: evidence from Mesozoic basalts and high-Mg andesites. Geochim. Cosmochim. Acta 67, 4373–4387.
Zhang, K.J., Tang, X.C., Wang, Y., Zhang, Y.X., 2011. Geochronology, geochemistry, and Nd isotopes of early Mesozoic bimodal volcanism in northern Tibet, western China: constraints on the exhumation of the central Qiangtang metamorphic belt. Lithos

121, 167–175.
Zhang, P.F., 2013. Geochemical Characteristics and Petrogenesis of the Volcanic Rocks from the Middle of the Yinshan Block. Master Degree Thesis.
Zhang, S.T., Wu, T.R., Xu, X., Byamba, J., Amarjargal, A., Wang, S.Q., Li, Z.Q., 2005. The significance of discovery of early Cretaceous shoshonite in central InnerMongolia. Geol. J. China Univ. 41, 212–218 (in Chinese with English abstract).
Zhao, G., Sun, M., Wilde, S.A., Li, S., 2005. Late Archean to Paleoproterozoic evolution of the North China Craton: key issues revisited. Precambrian Res. 136, 177–202.
Zheng, J.P., Griffin, W.L., O'Reilly, S.Y., Yang, J.S., Li, T.F., Zhang, M., Zhang, R.Y., Liou, J.G., 2006. Mineral chemistry of peridotites from Paleozoic, Mesozoic and Cenozoic lithosphere: constraints on mantle evolution beneath eastern China. J. Petrol. 47, 2233–2256.
Zhou, Y., Liang, X., Kröner, A., Cai, Y., Shao, T., Wen, S., Ellipsis Dong, C., 2015. Late Cretaceous lithospheric extension in SE China: constraints from volcanic rocks in Hainan Island. Lithos 232, 100–110.
Zhu, D.C., Zhao, Z.D., Niu, Y.L., Ellipsis Mo, X.X., 2012. Cambrian bimodal volcanism in the Lhasa Terrane, southern Tibet: record of an early Paleozoic Andean-type magmatic arc in the Australian proto-Tethyan margin. Chem. Geol. 328, 290–308.
Zindler, A., Hart, S., 1986. Chemical geodynamics. Annu. Rev. Earth Planet. Sci. 14, 493–571.
Zou, H.P., Zhang, K., Li, G., 2008. Cretaceous tectono-thermal event in the Ordos block: an Ar-Ar chronological evidence from basalt at Hangjin Banner, Inner Mongolia, North China Craton. Geotecton. Metallog. 32, 360–364 (in Chinese with English abstract).